Electromagnetic gyrokinetic simulation of turbulence in torus plasmas

Electromagnetic gyrokinetic simulation of turbulence in torus plasmas

A. ISHIZAWA†, S. MAEYAMA[1],
T.-H. WATANABE[2], H. SUGAMA, and N. NAKAJIMA

National Institute for Fusion Science, Toki, 509-5292, Japan
[1]Japan Atomic Energy Agency, Kashiwa, 277-8587 Japan
[2]Nagoya University, Nagoya 464-8602 Japan

(Received)

Gyrokinetic simulations of electromagnetic turbulence in magnetically confined torus plasmas including tokamak and heliotron/stellarator are reviewed. Numerical simulation of turbulence in finite beta plasmas is an important task for predicting performance of fusion reactors and a great challenge in computational science due to multiple spatio-temporal scales related to electromagnetic ion and electron dynamics. The simulation becomes further challenging in non-axisymmetric plasmas. In finite beta plasmas, magnetic perturbation appears and influences some key mechanisms of turbulent transport, which include linear instability and zonal flow production. Linear analysis shows that the ion-temperature gradient (ITG) instability, which is essentially an electrostatic instability, is unstable at low beta and its growth rate is reduced by magnetic field line bending at finite beta. On the other hand, the kinetic ballooning mode (KBM), which is an electromagnetic instability, is destabilized at high beta. In addition, trapped electron modes, electron temperature gradient modes, and micro-tearing modes can be destabilized. These instabilities are classified into two categories: ballooning parity and tearing parity modes. These parities are mixed by nonlinear interactions, so that, for instance, the ITG mode excites tearing parity modes. In the nonlinear evolution, the zonal flow shear acts to regulate the ITG driven turbulence at low-beta. On the other hand, at finite beta, interplay between the turbulence and zonal flows becomes complicated because the production of zonal flow is influenced by the finite beta effects. When the zonal flows are too weak, turbulence continues to grow beyond a physically relevant level of saturation in finite-beta tokamaks. Nonlinear mode coupling to stable modes can play a role in the saturation of finite beta ITG mode and KBM. Since there is a quadratic conserved quantity, evaluating nonlinear transfer of the conserved quantity from unstable modes to stable modes is useful for understanding the saturation mechanism of turbulence.

1. Introduction

Micro-turbulence causes anomalous transport of heat and particles in magnetically confined plasmas [1]. The plasma pressure normalized by the magnetic energy $\beta = 8\pi p/B^2$ is called plasma beta, and is one of the important parameters of fusion

† Email address for correspondence: ishizawa@nifs.ac.jp

plasmas because it is linked to the fusion reaction rate (Sec. 3.5 in [2] and Sec. 5.3 in [3]) and also related to the production of bootstrap current (Sec. 11.4 in [4]) that is important for steady state operations of tokamaks. Thus, the beta dependence of turbulent transport is one of the central issues in fusion plasma research. In order to understand the dependence, the influence of magnetic perturbation on the balance between zonal flow and micro-turbulence should be investigated. In addition, the validity of the Rechester-Rosenbluth model [5] describing direct effects of magnetic perturbation on heat transport should be understood.

Gyrokinetic simulation is a reliable tool for understanding and predicting turbulent transport in magnetically confined plasmas. The turbulent transport due to ion temperature gradient instability has been extensively studied by assuming the adiabatic response of electrons along the magnetic field line [6] (See Sec. 4.2). When we explore problems of turbulent transport at finite beta, we need to include magnetic perturbation and kinetic electrons because the current density is mainly carried by electrons. Including kinetic electrons to numerical simulations requires much more computational resources compared to the adiabatic electron simulations because the thermal velocity of electrons is much greater than the ion thermal velocity $v_{Te} = \sqrt{T_e/m_e} \gg v_{Ti} = \sqrt{T_i/m_i}$ when the ion and electron temperatures are comparable, and thus the parallel circulation time of electrons along the magnetic field line is much faster than that of ions. In order to capture such fast electron motion the time step is normally required to be small. In addition, the kinetic electron effect elongates the mode structure along the field line, and thus a large simulation domain along the field line is required. Large computational resources which meet the requirements are the reason why numerical simulations of turbulence based on the electromagnetic gyrokinetic model [7, 8, 9, 10, 11] are mainly carried out in the flux-tube geometry [12, 13, 14, 15, 16, 17, 18, 19, 20, 21, 22, 23, 24, 25] which is along a magnetic field line and is localized in the radial direction to reduce computational cost [26]. Although there are some gyrokinetic simulations on electromagnetic turbulence in global domain covering a whole torus plasma and also some electromagnetic gyrokinetic studies on space plasmas [27], we focus on gyrokinetic simulations in local flux-tube domain in this review.

Electromagnetic gyrokinetic simulations are applied to the studies of turbulent transport in finite-beta tokamak plasmas and the beta-scan is carried out [18, 19, 21]. In finite-beta tokamak plasmas the growth rate of the ion temperature gradient (ITG) instability is suppressed by magnetic field line bending as plasma beta increases [28] (Sec. 6). The production of zonal flow is also influenced by magnetic perturbation in finite beta plasmas [21]. The weak zonal flow leads to a situation in which instabilities continue to grow beyond a physically relevant level of saturation in finite-beta regime (Sec. 7.3) [22, 24]. This is in contrast with the ITG driven turbulence regulated by zonal flows in low-beta torus plasmas. The difficulties are related to the weak zonal flow production, and thus the production process of zonal structures is investigated [22, 24, 29, 30]. The identification of the saturation mechanism of microturbulence in regimes where zonal flow generation is weak at finite beta is one of the open issues.

Some properties of the gyrokinetic equations are useful for understanding the physics of numerical simulation results (Sec. 3). One is a quadratic conserved quantity of the electromagnetic gyrokinetic equation (Sec. 3.1). The saturation process of turbulence can be investigated by evaluating the nonlinear transfer of the quadratic quantity from unstable modes to stable modes in the Fourier mode space. Another

is the conservation of the parity symmetry of perturbation against the coordinate along the magnetic field line during the linear growth of instability (Sec. 3.3). The parity symmetry of magnetic perturbation is linked to the violation of magnetic surfaces, which enhances turbulent transport. The symmetry is broken through nonlinear interactions.

In high-beta torus plasmas, microturbulence can be driven by the kinetic ballooning mode (KBM) [28, 32, 33]. The difference between ITG turbulence at low beta and KBM turbulence is caused by zonal flow production. The mode structures of the ITG mode and KBM are similar in their linear growth phase. Both of them have a ballooning structure that appears around the outside of the torus, i.e., the bad curvature region. However, when the ITG mode and KBM grow, they exhibit significant differences from each other. The ITG mode produces zonal flows, and the flows regulate the amplitude of ITG turbulence at low beta. On the other hand, zonal flows in KBM turbulence are very weak, and thus it is difficult for KBM turbulence to become a saturated state compared with the low beta ITG turbulence. In fact, even MHD ballooning modes sometimes continue to grow without saturation by forming a finger-like structure. It is noticed that an MHD simulation corresponds to a very high-beta gyrokinetic simulation. Even though the zonal flow is normally weak, the KBM turbulence can be saturated at a physically relevant level when the electron temperature gradient is small and the beta value is just above the linear instability threshold. The saturation mechanism is related to the mode structure along the magnetic field line rather than zonal flow shear. Details of the mechanism are explained in Sec. 8.1.1.

We review micro-instability, micro-turbulence, and transport due to the turbulence in finite beta plasmas by reproducing the previous work cited in each section by means of the electromagnetic gyrokinetic simulation code GKV+ [34, 35, 36]. In Sec. 2, the electromagnetic gyrokinetic equation, Poisson equation, and Ampère's law are described. The conserved quantities of the gyrokinetic equation is presented in Sec. 3. Some difficulties of numerical simulations of the electromagnetic gyrokinetic equation are described in Sec. 4. Numerical setting is shown in Sec. 5. Linear instabilities are described in Sec. 6. Nonlinear evolution of turbulence is presented in Sec. 7. Saturation of KBM turbulence is discussed in Sec. 8. Magnetic islands and magnetic reconnection related to the turbulence is briefly reviewed in Sec. 9. Finally, summaries are given in Sec. 10.

2. Electromagnetic gyrokinetic equation

The electromagnetic gyrokinetic model for studying micro-turbulence in finite beta plasmas is described in this section [7, 8, 9, 10]. The distribution functions, which are governed by the kinetic equation

$$\left[\frac{\partial}{\partial t}+\mathbf{v}\cdot\nabla+\frac{q_s}{m_s}\left(\mathbf{E}+\frac{1}{c}\mathbf{v}\times\mathbf{B}\right)\cdot\frac{\partial}{\partial\mathbf{v}}\right]F_s=C_s(F_s), \tag{2.1}$$

can be divided into the Maxwellian part and a perturbed part $F_s = F_{Ms} + \delta f_s$ where $F_{Ms} = \frac{n_0}{(2\pi T_s/m_s)^{3/2}}\exp(-\frac{m_s v_\parallel^2}{2T_s} - \frac{\mu B}{T_s})$ and $\mathbf{v} = v_\parallel \mathbf{B}/B + \mathbf{v}_\perp$, and $\mu = m_s v_\perp^2/(2B)$ is the magnetic moment. The subscript s denotes particle species such as for ions $s = i$ and electrons $s = e$. In magnetically confined torus plasmas, a perturbation varies slowly along the magnetic field line, while it varies rapidly

perpendicular to the field line. The eikonal representation is useful for describing these fast and slow changes of the perturbation in the space as $\delta f_s(\mathbf{X}, v_\parallel, \mu, t) = \sum_{\mathbf{k}_\perp} \delta f_{s\mathbf{k}_\perp}(k_x, k_y, z, v_\parallel, \mu, t) \exp(iS_{\mathbf{k}_\perp})$, where $\nabla S_{\mathbf{k}_\perp} = \mathbf{k}_\perp = (k_x, k_y)$ and z is the coordinate along the magnetic field line. We can easily make the flute approximation $1/L \approx k_\parallel \ll k_\perp$ in terms of the eikonal representation [11], where L is the size of the plasma. In addition, the finite Larmor radius effects can be written in an analytic form when we use the eikonal representation. The gyrokinetic equation for perturbed ion and electron gyro-center distribution functions $\delta f_{s\mathbf{k}_\perp}$, the gyrokinetic Poisson equation for electrostatic potential $\phi_{\mathbf{k}_\perp}$, and gyrokinetic Ampère's law for parallel component of perturbed vector potential $A_{\parallel\mathbf{k}_\perp}$ are derived by assuming

$$\frac{\delta f_{s\mathbf{k}_\perp}}{F_{Ms}} \approx \frac{\rho_s}{L} \approx \frac{k_\parallel}{k_\perp} \approx \frac{\omega}{\Omega_s} \approx \frac{q_s\phi_{\mathbf{k}_\perp}}{T_s} \approx \frac{A_{\parallel\mathbf{k}_\perp}}{B\rho_s} \ll 1, \tag{2.2}$$

where $\rho_s = \frac{v_{Ts}}{\Omega_s}$ and $\Omega_s = \frac{q_s B}{m_s c}$. The equations are

$$\begin{aligned}
&\frac{\partial \delta f_{s\mathbf{k}_\perp}}{\partial t} + v_{Ts} v_\parallel (\mathbf{b}_s^* \cdot \nabla \delta f_s)_{\mathbf{k}_\perp} - v_{Ts}\mu \mathbf{b}\cdot\nabla B \frac{\partial \delta f_{s\mathbf{k}_\perp}}{\partial v_\parallel} \\
&= -i\mathbf{v}_{ds}\cdot\mathbf{k}_\perp \left(\delta f_{s\mathbf{k}_\perp} + \frac{q_s}{T_s} F_{Ms}\phi_{\mathbf{k}_\perp} J_{0s} \right) - (\tilde{\mathbf{v}}_{Es}\cdot\nabla\delta f_s)_{\mathbf{k}_\perp} \\
&\quad + i\mathbf{v}_{*s}\cdot\mathbf{k}_\perp \frac{q_s}{T_s} F_{Ms} \left(\phi_{\mathbf{k}_\perp} - v_{Ts} v_\parallel A_{\parallel\mathbf{k}_\perp} \right) J_{0s} + v_{Ts} v_\parallel \frac{q_s}{T_s} F_{Ms} E_{\parallel s\mathbf{k}_\perp} + C_s,
\end{aligned} \tag{2.3}$$

$$\lambda_{Di}^2 k_\perp^2 \phi_{\mathbf{k}_\perp} = \sum_s q_s \delta n_{s\mathbf{k}_\perp}^{(p)}, \tag{2.4}$$

$$k_\perp^2 A_{\parallel\mathbf{k}_\perp} = \frac{\beta_i}{2} \sum_s q_s v_{Ts} \delta u_{s\mathbf{k}_\perp}^{(p)}, \tag{2.5}$$

respectively, where $E_{\parallel s\mathbf{k}_\perp} = -(\mathbf{b}_s^*\cdot\nabla J_{0s}\phi)_{\mathbf{k}_\perp} - \frac{\partial}{\partial t} A_{\parallel\mathbf{k}_\perp} J_{0s}$, $\delta n_{s\mathbf{k}_\perp}^{(p)} = \int \delta f_{s\mathbf{k}_\perp} J_{0s} d^3v - \frac{q_s}{T_s}(1-\Gamma_{0s})\phi_{\mathbf{k}_\perp}$, $\delta u_{s\mathbf{k}_\perp}^{(p)} = \int v_\parallel \delta f_{s\mathbf{k}_\perp} J_{0s} d^3v$, are the parallel component of the perturbed electric field, the perturbed density measured at the particle position, and the parallel component of perturbed velocity measured at the particle position, respectively. Nonlinear terms are included in the convective derivative by perturbed E×B flow $(\tilde{\mathbf{v}}_{Es}\cdot\nabla f)_{\mathbf{k}_\perp} = [\phi J_{0s}, f]_{\mathbf{k}_\perp}$ and the parallel component of spatial gradient including magnetic perturbation $(\mathbf{b}_s^*\cdot\nabla f)_{\mathbf{k}_\perp} = \mathbf{b}\cdot\nabla f_{\mathbf{k}_\perp} + (\tilde{\mathbf{b}}_s\cdot\nabla f)_{\mathbf{k}_\perp} = \mathbf{b}\cdot\nabla f_{\mathbf{k}_\perp} - [A_\parallel J_{0s}, f]_{\mathbf{k}_\perp}$, where $\tilde{\mathbf{b}}_s = -\mathbf{b}\times i\mathbf{k}_\perp A_{\parallel\mathbf{k}_\perp} J_{0s}$. The unit vector of the equilibrium magnetic field is $\mathbf{b} = \mathbf{B}_0/B_0$, and $\mathbf{b}_s^* = \mathbf{b} + \tilde{\mathbf{b}}_s$ includes the perturbed part of the magnetic field, and the subscript 0 of the equilibrium magnetic field is omitted below. In the equation $[f, g]_{\mathbf{k}_\perp} = \sum_{\mathbf{k}'_\perp, \mathbf{k}''_\perp} \delta_{\mathbf{k}_\perp, \mathbf{k}'_\perp + \mathbf{k}''_\perp} \mathbf{b}\cdot\mathbf{k}'_\perp \times \mathbf{k}''_\perp f_{\mathbf{k}'_\perp} g_{\mathbf{k}''_\perp}$ and $J_{0s} = J_0(\rho_s k_\perp)$ are the Poisson bracket and the zeroth order Bessel function, respectively. The magnetic drift, the diamagnetic drift, and the perturbed E×B drift velocities are $\mathbf{v}_{ds} = \frac{1}{q_s B}\mathbf{b}\times(\mu\nabla B + m_s v_\parallel^2 \mathbf{b}\cdot\nabla\mathbf{b})$, $\mathbf{v}_{*s} = \frac{T_s}{q_s B}\mathbf{b}\times\nabla\ln F_{Ms}$, and $\tilde{\mathbf{v}}_{Es\mathbf{k}_\perp} = -\frac{1}{B}(i\mathbf{k}_\perp\phi_{\mathbf{k}_\perp} J_{0s})\times\mathbf{b}$, respectively. The collision operator is denoted by $C_s(h_{s\mathbf{k}_\perp})$, where $h_{s\mathbf{k}_\perp} = \delta f_{s\mathbf{k}_\perp} + \frac{q_s}{T_s}\phi_{\mathbf{k}_\perp} J_{0s} F_{Ms}$ is the non-adiabatic part of the perturbed part of the gyro-center distribution function. The normalizations used in the equations are $(tv_{Ti}/L_n,\ \mathbf{k}_\perp\rho_{Ti},\ v_\parallel/v_{Ts},\ F_{Ms}v_{Ts}^3/n_0,\ \delta f_s L_n v_{Ts}^3/(\rho_{Ti} n_0),\ \phi e L_n/(\rho_{Ti} T_i),\ A_\parallel L_n/(\rho_{Ti}^2 B_0),\ m_s/m_i,\ T_s/T_i,\ n/n_0,\ B/B_0,\ q_s/e,\ \lambda_{Di}/\rho_{Ti}) \to (t,\ \mathbf{k}_\perp,\ v_{\parallel s},\ F_{Ms},\ \delta f_s,\ \phi,\ A_\parallel,\ M_s,\ T_s,\ n,\ B,\ q_s,\ \lambda_{Di})$, where $\lambda_{Di} = \sqrt{T_i/(4\pi e^2 n_0)}$ and $v_{Ts} = \sqrt{T_s/m_s}$, and the leading order of Larmor radius ρ_i is written as

$\rho_{Ti} = v_{Ti}/\Omega_i$. The dimensional form of the gyrokinetic equation is shown in Appendix A.

The second term in the l.h.s. of Eq. (2.3) represents the parallel convection and is important for parallel streaming, the Landau damping, and the magnetic field line bending effect, which stabilizes the ITG mode at finite beta, as shown in Appendix B. The first term in the r.h.s. is the magnetic drift term and causes instability by combining with the diamagnetic drift term (the fourth term in the r.h.s.). The second term in the r.h.s. is the parallel acceleration by the perturbed electric field. The third term in the r.h.s. is the mirror term causing particle trapping in a weak magnetic field region. The polarization effects due to finite Larmor radius is represented by $1-\Gamma_{0s}$ term in the Poisson equation through $n^{(p)}_{s\mathbf{k}_\perp}$, where $\Gamma_{0s} = e^{-\rho_s^2 k_\perp^2} I_0(\rho_s^2 k_\perp^2)$ and I_0 is the zeroth order modified Bessel function. The parallel component of the perturbed magnetic field and the finite beta term in the magnetic drift velocity are neglected by assuming that the plasma beta is not so high and does not affect the equilibrium. Temperature and density gradients are assumed to be uniform in local simulations and direct to the radial direction x, and the temperature gradient is represented by the parameter $\eta_s = L_n/L_{T_s}$ in terms of density scale length $L_n = -(d\ln n/dx)^{-1}$ and temperature scale lengths $L_{Ts} = -(d\ln T_s/dx)^{-1}$.

It is noted that the ion beta $\beta_i = 8\pi n_0 T_i/B_0^2$ appears only in the Ampère's law Eq. (2.5) and is the relevant parameter representing the electromagnetic effect, because the magnetic perturbation $A_\parallel$ disappears when $\beta_i = 0$.

3. Conserved quantities

3.1. Conservation of quadratic quantities (Entropy balance equation)

There is a quadratic conserved quantity called the entropy variable [37]. The name comes from the fact that it is the perturbed part of the Shanon entropy $\delta S_s = S_s - S_{s0}$, where $S_s = -\langle \int F_s \ln F_s d^3v\rangle$, $F_s = F_{Ms} + \delta f_s$, $S_{s0} = -\langle \int F_{Ms} \ln F_{Ms} d^3v\rangle$, and $\langle F_s\rangle = F_{Ms}$. The equation governing the quadratic form of the perturbed part of the distribution function $\delta S_s = \left\langle \int d^3v \frac{|\delta f_s|^2}{2F_{Ms}} \right\rangle$ is obtained by multiplying $h^*_{s\mathbf{k}_\perp} = \delta f^*_{s\mathbf{k}_\perp} + \frac{q_s}{T_s}\phi^*_{\mathbf{k}_\perp} J_{0s} F_{Ms}$ with Eq. (2.3), integrating over the velocity space, and making flux surface average with Eqs. (2.4) and (2.5) (Details are given in Appendix C), where $*$ denotes the complex conjugate. The equation is written as

$$\frac{d}{dt}\left(\sum_s \delta S_s + W_{es} + W_{em}\right) = \sum_s \left(\frac{\Theta_s}{L_{Ts}} + \frac{T_s\Gamma_s}{L_{ps}} + D_s\right), \tag{3.1}$$

where $1/L_{ps} = 1/L_{Ts} + 1/L_n$, $\Theta_s = \Theta_{es,s} + \Theta_{em,s}$, $\Gamma_s = \Gamma_{es,s} + \Gamma_{em,s}$, $\delta S_s = \sum_{\mathbf{k}_\perp} \delta S_{s\mathbf{k}_\perp}$, $W_{es} = \sum_{\mathbf{k}_\perp} W_{es\mathbf{k}_\perp}$, $W_{em} = \sum_{\mathbf{k}_\perp} W_{em\mathbf{k}_\perp}$, $\Theta_{es,s} = \sum_{\mathbf{k}_\perp} \Theta_{es,s\mathbf{k}_\perp}$, $\Theta_{em,s} = \sum_{\mathbf{k}_\perp} \Theta_{em,s\mathbf{k}_\perp}$, $\Gamma_{es,s} = \sum_{\mathbf{k}_\perp} \Gamma_{es,s\mathbf{k}_\perp}$, $\Gamma_{em,s} = \sum_{\mathbf{k}_\perp} \Gamma_{em,s\mathbf{k}_\perp}$. In the equations

$$\delta S_{s\mathbf{k}_\perp} = \left\langle \int d^3v \frac{T_s |\delta f_{s\mathbf{k}_\perp}|^2}{2F_{Ms}} \right\rangle, \tag{3.2}$$

$$D_{s\mathbf{k}_\perp} = \left\langle \int d^3v \frac{T_s}{F_{Ms}} \left(\delta f^*_{s\mathbf{k}_\perp} + \frac{q_s}{T_s}\phi^*_{\mathbf{k}_\perp} J_{0s} F_{Ms}\right) C_s(h_{s\mathbf{k}_\perp}) \right\rangle, \tag{3.3}$$

$$W_{es\mathbf{k}_\perp} = \left\langle \left(\lambda_{Di}^2 k_\perp^2 + \sum_s \frac{q_s^2}{T_s}[1-\Gamma_0(b_{sk})] \right) \frac{|\phi_{\mathbf{k}_\perp}|^2}{2} \right\rangle, W_{em\mathbf{k}_\perp} = \left\langle \frac{2}{\beta_i} \frac{k_\perp^2 |A_{\parallel \mathbf{k}_\perp}|^2}{2} \right\rangle, \tag{3.4}$$

$$\Theta_{es,s\mathbf{k}_\perp} = \left\langle Re \left[\left(\frac{1}{2}\delta\hat{p}_{\parallel s\mathbf{k}_\perp} + \delta\hat{p}_{\perp s\mathbf{k}_\perp} - \frac{5}{2}T_s\delta\hat{n}_{s\mathbf{k}_\perp} \right) \left(\frac{-ik_y\phi_{\mathbf{k}_\perp}}{B} \right)^* \right] \right\rangle, \tag{3.5}$$

$$\Theta_{em,s\mathbf{k}_\perp} = \left\langle Re \left[\left(\frac{1}{2}\delta\hat{q}_{\parallel s\mathbf{k}_\perp} + \delta\hat{q}_{\perp s\mathbf{k}_\perp} \right) \left(\frac{ik_y A_{\parallel \mathbf{k}_\perp}}{B} \right)^* \right] \right\rangle, \tag{3.6}$$

$$\Gamma_{es,s\mathbf{k}_\perp} = \left\langle Re \left[\delta\hat{n}_{s\mathbf{k}_\perp} \left(\frac{-ik_y\phi_{\mathbf{k}_\perp}}{B} \right)^* \right] \right\rangle, \Gamma_{em,s\mathbf{k}_\perp} = \left\langle Re \left[\delta\hat{u}_{s\mathbf{k}_\perp} \left(\frac{ik_y A_{\parallel \mathbf{k}_\perp}}{B} \right)^* \right] \right\rangle, \tag{3.7}$$

are the entropy variable, the collisional dissipation, the electrostatic energy including the polarization field, the magnetic energy, the entropy production due to the turbulent thermal transport flux caused by the electrostatic and the magnetic perturbations, the entropy production due to the particle transport flux caused by the electrostatic and the magnetic perturbations. The flux surface average is represented by $\langle\rangle$. The l.h.s. of Eq. (3.1) is called the generalized energy in Ref. [27]. It is remarked that Eqs. (3.5)-(3.7) correspond to the free energy of instabilities. In these equations

$$\delta\hat{n}_{s\mathbf{k}_\perp} = \int \delta f_{s\mathbf{k}_\perp} J_{0s} d^3v, \qquad \delta\hat{u}_{s\mathbf{k}_\perp} = \int v_\parallel \delta f_{s\mathbf{k}_\perp} J_{0s} d^3v, \tag{3.8}$$

$$\delta\hat{p}_{\parallel s\mathbf{k}_\perp} = \int m_s v_\parallel^2 \delta f_{s\mathbf{k}_\perp} J_{0s} d^3v, \qquad \delta\hat{p}_{\perp s\mathbf{k}_\perp} = \int \mu B \delta f_{s\mathbf{k}_\perp} J_{0s} d^3v, \tag{3.9}$$

$$\delta\hat{q}_{\parallel s\mathbf{k}_\perp} = \int m_s v_\parallel^3 \delta f_{s\mathbf{k}_\perp} J_{0s} d^3v - 3T_s\delta\hat{u}_{s\mathbf{k}_\perp}, \tag{3.10}$$

and

$$\delta\hat{q}_{\perp s\mathbf{k}_\perp} = \int \mu B v_\parallel \delta f_{s\mathbf{k}_\perp} J_{0s} d^3v - T_s\delta\hat{u}_{s\mathbf{k}_\perp}. \tag{3.11}$$

We can evaluate the transfer of entropy (free energy) from a particle species to the other species by evaluating $R_s = d\delta S_s/dt - \Theta_s/L_{Ts} - \Gamma_s T_s/L_{ps} - D_s$ because Eq. (3.1) can be written as

$$\sum_s R_s + \frac{d}{dt}(W_{es} + W_{em}) = 0, \tag{3.12}$$

in terms of R_s. For instance, the entropy is transferred from ions to electrons in the slab ITG turbulence [38] and in the KBM turbulence [39].

Some conclusions can be derived from the entropy balance equations without carrying out numerical simulations. When we have a statistical steady state, the time derivative terms in Eq. (3.1) are very small, and the entropy production due to the transport flux should balance with collisional dissipation terms [40]

$$\sum_s \left(\frac{\Theta_s}{L_{Ts}} + \frac{T_s\Gamma_s}{L_{ps}} \right) = -\sum_s D_s. \tag{3.13}$$

It is to be noted that the ion and electron particle flux caused by electrostatic (magnetic) perturbation are the same, $\Gamma_{es,i} = \Gamma_{es,e}$ ($\Gamma_{em,i} = \Gamma_{em,e}$), so that $\Gamma_i =$

$\Gamma_e \equiv \Gamma$, because of the Poisson equation Eq. (2.4) (the Ampère's law Eq. (2.5)) [41].

3.2. Nonlinear entropy transfer in the Fourier space

The entropy balance equation for a Fourier mode $\mathbf{k}_\perp$ is written as

$$\frac{d}{dt}\left(\sum_s \delta S_{s\mathbf{k}_\perp} + W_{es\mathbf{k}_\perp} + W_{em\mathbf{k}_\perp}\right) = \sum_s \left(\mathcal{T}_{s\mathbf{k}_\perp} + \frac{\Theta_{s\mathbf{k}_\perp}}{L_{Ts}} + \frac{T_s \Gamma_{s\mathbf{k}_\perp}}{L_{ps}} + D_{s\mathbf{k}_\perp}\right), \tag{3.14}$$

where

$$\mathcal{T}_{s\mathbf{k}_\perp} = \sum_{\mathbf{k}'_\perp} \sum_{\mathbf{k}''_\perp} \mathcal{T}_s(\mathbf{k}_\perp; \mathbf{k}'_\perp, \mathbf{k}''_\perp) \tag{3.15}$$

originates from the nonlinear terms in Eq. (2.3). Equation (3.14) implies that the saturation mechanism of turbulence can be studied by evaluating the nonlinear entropy transfer function

$$\mathcal{T}(\mathbf{k}_\perp; \mathbf{k}'_\perp, \mathbf{k}''_\perp) = \sum_s \mathcal{T}_s(\mathbf{k}_\perp; \mathbf{k}'_\perp, \mathbf{k}''_\perp), \tag{3.16}$$

where

$$\mathcal{T}_s(\mathbf{k}_\perp; \mathbf{k}'_\perp, \mathbf{k}''_\perp) = \mathrm{Re}\left\langle \int d^3v \frac{T_s h_{s\mathbf{k}_\perp}}{2F_{Ms}} \delta_{\mathbf{k}_\perp, -\mathbf{k}'_\perp - \mathbf{k}''_\perp} \mathbf{b} \cdot \mathbf{k}'_\perp \times \mathbf{k}''_\perp (\chi_{s\mathbf{k}'_\perp} h_{s\mathbf{k}''_\perp} - h_{s\mathbf{k}'_\perp} \chi_{s\mathbf{k}''_\perp}) \right\rangle, \tag{3.17}$$

where $h_{s\mathbf{k}_\perp} = \delta f_{s\mathbf{k}_\perp} + \frac{q_s}{T_s}\phi_{\mathbf{k}_\perp} J_{0s} F_{Ms}$ is the non-adiabatic part of the perturbed part of the gyro-center distribution function and $\chi_{s\mathbf{k}_\perp} = (\phi_{\mathbf{k}_\perp} - v_\parallel A_{\parallel\mathbf{k}_\perp}) J_{0s}$ is the generalized potential [42]. In the electrostatic limit ($A_\parallel \to 0$), the transfer function is reduced to that in Ref. [43]. The transfer function satisfies the detailed balance equation, $\mathcal{T}_s(\mathbf{k}_\perp; \mathbf{k}'_\perp, \mathbf{k}''_\perp) + \mathcal{T}_s(\mathbf{k}'_\perp; \mathbf{k}''_\perp, \mathbf{k}_\perp) + \mathcal{T}_s(\mathbf{k}''_\perp; \mathbf{k}_\perp, \mathbf{k}'_\perp) = 0$, and $\mathcal{T}_s(\mathbf{k}_\perp; \mathbf{k}'_\perp, \mathbf{k}''_\perp) = \mathcal{T}_s(\mathbf{k}_\perp; \mathbf{k}''_\perp, \mathbf{k}'_\perp) = \mathcal{T}_s(-\mathbf{k}_\perp; -\mathbf{k}'_\perp, -\mathbf{k}''_\perp)$. The detailed balance equation leads to the relation $\sum_{\mathbf{k}_\perp} \mathcal{T}_{s\mathbf{k}_\perp} = 0$. The diagram of the nonlinear entropy transfer illustrated in Fig. 1 (a) shows an example of nonlinear interaction among $\mathbf{k}_\perp$, $\mathbf{k}'_\perp$, and $\mathbf{k}''_\perp$ modes. The $\mathbf{k}_\perp$ and $\mathbf{k}'_\perp$ modes lose the free energy and $\mathbf{k}''_\perp$ mode gains the free energy. An example of the entropy transfer process in the ITG turbulence regulated by zonal flows is illustrated in Fig. 1 (b) in terms of the diagram. There are three arrows connected to a triangle. The first arrow starting from the ITG mode $\mathbf{k}_{\perp\mathrm{ITG}} = (k_{x\mathrm{ITG}}, k_{y\mathrm{ITG}})$ and pointing to the triangle represents the transfer function $\mathcal{T}(\mathbf{k}_{\perp\mathrm{ITG}}; \mathbf{k}'_{\perp\mathrm{ZF}}, \mathbf{k}''_\perp) < 0$, which implies that the entropy is transferred from the ITG mode with $\mathbf{k}_{\perp\mathrm{ITG}} = (k_{x\mathrm{ITG}}, k_{y\mathrm{ITG}})$ to the zonal flow with $\mathbf{k}'_{\perp\mathrm{ZF}} = (k_{x\mathrm{ZF}}, 0)$ and a higher radial wavenumber mode with $\mathbf{k}''_\perp = (-k_{x\mathrm{ITG}} - k_{x\mathrm{ZF}}, -k_{y\mathrm{ITG}})$, where $f(k_x, k_y) = f(-k_x, -k_y)^*$ is used to satisfy $\mathbf{k}_\perp + \mathbf{k}'_\perp + \mathbf{k}''_\perp = \mathbf{0}$. The second arrow starting from the triangle and pointing to "Zonal flow $(k_{x\mathrm{ZF}}, 0)$" represents the transfer function $\mathcal{T}(\mathbf{k}'_{\perp\mathrm{ZF}}; \mathbf{k}''_\perp, \mathbf{k}_{\perp\mathrm{ITG}}) > 0$, which presents that the entropy is transferred to the zonal flow. The third arrow starting from the triangle and pointing to a higher radial wavenumber mode represents the transfer function $\mathcal{T}(\mathbf{k}''_\perp; \mathbf{k}_{\perp\mathrm{ITG}}, \mathbf{k}_{\perp\mathrm{ZF}}{}') > 0$, which implies that the entropy of the ITG mode is transferred into a higher radial wavenumber mode $\mathbf{k}''_\perp = (-k_{x\mathrm{ITG}} - k_{x\mathrm{ZF}}, -k_{y\mathrm{ITG}})$. It is remarked that the transfer to the zonal flow is significant in the saturation of the growth of the ITG mode. On the other hand, the transfer to the zonal flow is small in the steady state of the turbulence, and the

entropy is mainly transferred from the ITG mode to the higher radial wavenumber mode through the interaction with the zonal flow. The diagram illustrated in Fig. 1 (b) presents a typical transfer process of the entropy in the ITG turbulence with the adiabatic electrons, which is shown in Fig. 8 of Ref. [43]. The transfer function can be used to study the zonal flow production process and the saturation process of microturbulence, as shown in Sec. 7.1.

3.3. Conservation of parity

Here we discuss the parity symmetry of the gyrokinetic equation Eq. (2.3) against the coordinate along the magnetic field line. The parity transformation is the inversion of the coordinate direction along the magnetic field line in the magnetic field coordinate as illustrated in Fig. 1 of Ref. [45]. The linearized gyrokinetic equation is invariant under parity transformation $z \to -z$, $v_\parallel \to -v_\parallel$, $\theta_k \to -\theta_k$ ($k_x \to -k_x$) as shown below.

In order to understand the invariance, we rewrite the gyrokinetic equation Eq. (2.3) in terms of the non-adiabatic part of the perturbed part of gyro-center distribution function $h_{s\mathbf{k}_\perp} = \delta f_{s\mathbf{k}_\perp} + q_s \frac{F_{Ms}}{T_s}\phi_{\mathbf{k}_\perp} J_{0s}$, as

$$\frac{\partial h_{s\mathbf{k}_\perp}}{\partial t} = -i\mathbf{v}_{ds}\cdot\mathbf{k}_\perp h_{s\mathbf{k}_\perp} - v_{Ts}[H, h_{s\mathbf{k}_\perp}]_\parallel + q_s\frac{F_{Ms}}{T_s}\frac{\partial \chi_{s\mathbf{k}_\perp}}{\partial t} + i\mathbf{v}_{*s}\cdot\mathbf{k}_\perp q_s\frac{F_{Ms}}{T_s}\chi_{s\mathbf{k}_\perp} + [\chi_s, h_s]_{\mathbf{k}_\perp} + C_s(h_{s\mathbf{k}_\perp}), \tag{3.18}$$

where $\chi_{s\mathbf{k}_\perp} = (\phi_{\mathbf{k}_\perp} - v_{Ts}v_\parallel A_{\parallel\mathbf{k}_\perp})J_{0s}$ is the generalized potential, $[H, h_{s\mathbf{k}_\perp}]_\parallel \equiv \nabla_\parallel H\frac{\partial h_{s\mathbf{k}_\perp}}{\partial v_\parallel} - \frac{\partial H}{\partial v_\parallel}\nabla_\parallel h_{s\mathbf{k}_\perp} = v_\parallel\nabla_\parallel h_{s\mathbf{k}_\perp} - \mu\nabla_\parallel B\frac{\partial h_{s\mathbf{k}_\perp}}{\partial v_\parallel}$, $H = v_\parallel^2/2 + \mu B$, and $\nabla_\parallel = \mathbf{b}\cdot\nabla$. The Poisson equation and the Ampère's law (Eqs. (2.4) and (2.5)) are

$$\lambda_{Di}^2 k_\perp^2 \phi_{\mathbf{k}_\perp} = \sum_s q_s\left(\int h_{s\mathbf{k}_\perp} J_{0s} d^3v - \frac{q_s}{T_s}\phi_{\mathbf{k}_\perp}\right), \tag{3.19}$$

$$k_\perp^2 A_{\parallel\mathbf{k}_\perp} = \frac{\beta_i}{2}\sum_s q_s v_{Ts}\int v_\parallel h_{s\mathbf{k}_\perp} J_{0s} d^3v. \tag{3.20}$$

We assume that the magnetic field is invariant under the transformation $B(-z) = B(z)$. The squarer of the perpendicular wavenumber $k_\perp^2 = k_y^2[1 + \hat{s}^2(\theta - \theta_k)^2] = (k_x + \hat{s}zk_y)^2 + k_y^2$ is invariant under parity, where $\theta_k = -k_x/(k_y\hat{s})$ is the ballooning angle. We have $\nabla_\parallel \to -\nabla_\parallel$, $\mathbf{v}_{ds}\cdot\mathbf{k}_\perp \to \mathbf{v}_{ds}\cdot\mathbf{k}_\perp$, $\mathbf{v}_{*s}\cdot\mathbf{k}_\perp \to \mathbf{v}_{*s}\cdot\mathbf{k}_\perp$, $F_{Ms} \to F_{Ms}$, $C_s \to C_s$ under the transformation. We can confirm the invariance of magnetic and diamagnetic drift terms, for instance, for a large aspect ratio tokamak with concentric magnetic surface $\mathbf{v}_{*s}\cdot\mathbf{k}_\perp = k_y\frac{-T_s}{q_s L_n B}[1 + (\frac{v_\parallel^2}{2} + \mu B - \frac{3}{2})\eta_s]$ and $\mathbf{v}_{ds}\cdot\mathbf{k}_\perp = \frac{-T_s}{q_s RB}(v_\parallel^2 + \mu B)\left(k_x\sin z + k_y(\cos z + \hat{s}z\sin z)\right)$. It is noticed that the Poisson equation and Ampère's law (Eqs. (3.19) and (3.20)) imply that the parity of electrostatic potential is the same as that of the distribution function, while the parallel component of the vector potential has the opposite parity as the distribution function. Hence, the linearized gyrokinetic equation is invariant under the parity. By utilizing the invariance for the parity transformation, the perturbed distribution function can be divided into the even and the odd parity parts

$$\delta f_{s\mathbf{k}_\perp} = \delta f^+_{s\mathbf{k}_\perp} + \delta f^-_{s\mathbf{k}_\perp}, \tag{3.21}$$

where

$$\delta f^{+}_{s\mathbf{k}_\perp} = \frac{1}{2}\left\{\delta f_{s\mathbf{k}_\perp}(z, v_\parallel, k_x) + \delta f_{s\mathbf{k}_\perp}(-z, -v_\parallel, -k_x)\right\}, \tag{3.22}$$

$$\delta f^{-}_{s\mathbf{k}_\perp} = \frac{1}{2}\left\{\delta f_{s\mathbf{k}_\perp}(z, v_\parallel, k_x) - \delta f_{s\mathbf{k}_\perp}(-z, -v_\parallel, -k_x)\right\}. \tag{3.23}$$

The even parity mode does not change the sign of the perturbed distribution function against the parity transformation $\delta f^{+}_{s\mathbf{k}_\perp}(-z, -v_\parallel, -k_x) = \delta f^{+}_{s\mathbf{k}_\perp}(z, v_\parallel, k_x)$ and is called the ballooning parity mode, while the odd parity mode changes the sign of the distribution function $\delta f^{-}_{s\mathbf{k}_\perp}(-z, -v_\parallel, -k_x) = -\delta f^{-}_{s\mathbf{k}_\perp}(z, v_\parallel, k_x)$ and is called the tearing parity mode. The parities of perturbations are summarized in table 1. The parity is conserved during the linear growth of instabilities because the linearized gyrokinetic equation is invariant.

We have seen that the linearized gyrokinetic equation is invariant under the parity transformation. The parity is discussed in relation with the momentum transport [44, 45], and it is also useful for understanding the mode structure of instabilities especially in the electromagnetic simulations. Instabilities are classified into two groups: ballooning parity modes and tearing parity modes. The former includes the ITG mode, the trapped electron mode (TEM) mode, the electron temperature gradient mode, and the KBM, while the latter includes the micro-tearing mode. Typically, the most unstable mode has zero ballooning angle $\theta_k = 0$, i.e., it has no radial wave number $k_x = 0$, where $k_x = -k_y \hat{s}\theta_k$. We will see the typical profile of perturbations along the field line for the zero ballooning angle case $k_x = 0$ in Sec. 6.

The parity of perturbation is important in electromagnetic calculations because it is linked to the violation of magnetic surface. A magnetic field line is obtained by integrating the equation $\frac{dx}{B_x} = \frac{dy}{B_y} = \frac{dz}{B_z}$. The radial position of the field line is represented by $\int dx = \int \frac{B_x}{B_z} dz = \int \frac{\tilde{b_x}}{B_0} dz = \int \frac{ik_y A_\parallel}{B_0} dz$. It is considered that the magnetic surface is broken, when the radial position of a magnetic field line, which starts from one edge of the simulation box, does not go back to the original radial position at the another edge. Thus, the violation of the magnetic surface occurs, when the perturbation has the tearing parity and the integral of $A_\parallel$ along the field line does not vanish $\int_{-\infty}^{\infty} A^{-}_{\parallel\mathbf{k}_\perp} dz \neq 0$. On the other hand, the violation does not occur, when the perturbation has the ballooning parity $\int_{-\infty}^{\infty} A^{+}_{\parallel\mathbf{k}_\perp} dz = 0$.

The nonlinear term in the gyrokinetic equation causes interaction between different parity modes. The even/odd part of the nonlinear term in Eq. (3.18) is written as

$$[\chi_s, h_s]^{\pm}_{\mathbf{k}_\perp} = \frac{1}{2}\sum_{\mathbf{k}'_\perp, \mathbf{k}''_\perp} \delta_{\mathbf{k}_\perp, \mathbf{k}'_\perp + \mathbf{k}''_\perp} \mathbf{b}\cdot\mathbf{k}'_\perp \times \mathbf{k}''_\perp \Big\{\chi_{s\mathbf{k}'_\perp}(z, v_\parallel, k'_x) h_{s\mathbf{k}''_\perp}(z, v_\parallel, k''_x) \mp \chi_{s\mathbf{k}'_\perp}(-z, -v_\parallel, -k'_x) h_{s\mathbf{k}''_\perp}(-z, -v_\parallel, -k''_x)\Big\}. \tag{3.24}$$

We have $[\chi^+_s, h^+_s]^+_{\mathbf{k}_\perp} = 0$, $[\chi^-_s, h^-_s]^+_{\mathbf{k}_\perp} = 0$, $[\chi^+_s, h^-_s]^-_{\mathbf{k}_\perp} = 0$, $[\chi^-_s, h^+_s]^-_{\mathbf{k}_\perp} = 0$, $[\chi^+_s, h^-_s]^+_{\mathbf{k}_\perp} = [\chi^+_s, h^-_s]_{\mathbf{k}_\perp} \neq 0$, $[\chi^-_s, h^+_s]^+_{\mathbf{k}_\perp} = [\chi^-_s, h^+_s]_{\mathbf{k}_\perp} \neq 0$, $[\chi^+_s, h^+_s]^-_{\mathbf{k}_\perp} = [\chi^+_s, h^+_s]_{\mathbf{k}_\perp} \neq 0$, $[\chi^-_s, h^-_s]^-_{\mathbf{k}_\perp} = [\chi^-_s, h^-_s]_{\mathbf{k}_\perp} \neq 0$. Thus, the nonlinear terms in the gyrokinetic equation mix the parities. The parity mixing is important for the production of magnetic perturbation that violates the magnetic surface, as shown in Sec. 7.4.

	$\delta f_{s\mathbf{k}_\perp}$	$\phi_{\mathbf{k}_\perp}$	$A_{\parallel\mathbf{k}_\perp}$	$\chi_{s\mathbf{k}_\perp}$	$h_{s\mathbf{k}_\perp}$
Ballooning parity (+)	even	even	odd	even	even
Tearing parity (−)	odd	odd	even	odd	odd

Table 1. Parities of perturbations, where $\chi_{s\mathbf{k}_\perp} = (\phi_{\mathbf{k}_\perp} - v_{Ts}v_\parallel A_{\parallel\mathbf{k}_\perp})J_{0s}$ and $h_{s\mathbf{k}_\perp} = \delta f_{s\mathbf{k}_\perp} + q_s\frac{F_{Ms}}{T_s}\phi_{\mathbf{k}_\perp}J_{0s}$.

4. Difficulties of electromagnetic gyrokinetic simulations

4.1. Cancellation problem

The gyrokinetic equation Eq. (2.3) includes not only the time derivative of the gyro-center distribution function $\delta f_{s\mathbf{k}_\perp}$ but also the time derivative of $A_{\parallel\mathbf{k}_\perp}$, which is the induction part of the electric field. In numerical simulations, we normally use a variable

$$\delta f^{(h)}_{s\mathbf{k}_\perp} = \delta f_{s\mathbf{k}_\perp} - q_s\frac{F_{Ms}}{T_s}v_{Ts}v_\parallel J_{0s}A_{\parallel\mathbf{k}_\perp} \tag{4.1}$$

$$= h_{s\mathbf{k}_\perp} - q_s\frac{F_{Ms}}{T_s}\chi_{s\mathbf{k}_\perp}, \tag{4.2}$$

to eliminate $\frac{\partial A_\parallel}{\partial t}$ term, so that the gyrokinetic equation contains one time derivative term $\frac{\partial \delta f^{(h)}_{s\mathbf{k}_\perp}}{\partial t}$ as

$$\frac{\partial \delta f^{(h)}_{s\mathbf{k}_\perp}}{\partial t} + \left(i\mathbf{v}_{ds}\cdot\mathbf{k}_\perp + v_{Ts}v_\parallel\mathbf{b}\cdot\nabla - v_{Ts}\mu\mathbf{b}\cdot\nabla B\frac{\partial}{\partial v_\parallel}\right)\left(\delta f^{(h)}_{s\mathbf{k}_\perp} + q_s\frac{F_{Ms}}{T_s}\chi_{s\mathbf{k}_\perp}\right)$$
$$= i\mathbf{v}_{*s}\cdot\mathbf{k}_\perp q_s\frac{F_{Ms}}{T_s}\chi_{s\mathbf{k}_\perp} - [\chi_s, f^{(h)}_s]_{\mathbf{k}_\perp} + C_s(h_{s\mathbf{k}_\perp}), \tag{4.3}$$

where $\chi_{s\mathbf{k}_\perp} = (\phi_{\mathbf{k}_\perp} - v_{Ts}v_\parallel A_{\parallel\mathbf{k}_\perp})J_{0s}$ is the generalized potential. By numerically solving Eq. (4.3) we have $\delta f^{(h)}_{s\mathbf{k}_\perp}(t+\Delta t)$ from $\delta f^{(h)}_{s\mathbf{k}_\perp}(t)$, $\phi_{\mathbf{k}_\perp}(t)$, and $A_{\parallel\mathbf{k}_\perp}(t)$. In order to obtain $\phi_{\mathbf{k}_\perp}(t+\Delta t)$ and $A_{\parallel\mathbf{k}_\perp}(t+\Delta t)$, we must solve the Poisson and Ampere equations Eqs. (2.4) and (2.5). Substituting Eq. (4.1) into the Poisson equation yields

$$\lambda_{Di}^2k_\perp^2\phi_k = \sum_s q_s\left(\int \delta f^{(h)}_{sk}J_{0s}d^3v - \frac{q_s}{T_s}(1-\Gamma_{0s})\phi_k\right), \tag{4.4}$$

which has the same form as Eq. (2.4) because $\int F_{Ms}v_\parallel J_{0s}d^3v = 0$. On the other hand, the form of Ampère's law is modified to

$$\left(k_\perp^2 + \beta_i\sum_s\frac{q_s^2}{m_s}\int v_\parallel^2J_{0s}^2F_{Ms}d^3v\right)A_{\parallel k} = \beta_i\sum_s q_s\int v_\parallel\delta f^{(h)}_{sk}J_{0s}d^3v, \tag{4.5}$$

where the velocity space integral in the l.h.s. can be represented by the analytic form $\int v_\parallel^2J_{0s}^2F_{Ms}d^3v = \Gamma_{0s}$.

The cancellation problem stems from the fact that the second term is much larger than the first term in the l.h.s. of Eq. (4.1) for electrons $q_e\frac{F_{Ms}}{T_s}v_{Te}v_\parallel J_{0e}A_{\parallel k} \gg \delta f_{ek}$. The contribution of the second term of Eq. (4.1) $-q_e\frac{F_{Me}}{T_e}v_{Te}v_\parallel J_{0e}A_{\parallel k}$ in the r.h.s. of Eq. (4.5) should cancel out the second term of l.h.s. of Eq. (4.5). In practice, errors of the cancellation of the two terms can be comparable with the first term of the l.h.s. of Eq. (4.5) and lead to numerical instabilities. The numerical instability is called the cancellation problem and occurs when we evaluate the second term

in the l.h.s. of Eq. (4.5) by the analytic form Γ_{0s}. The cancellation problem can be avoided by integrating the two terms in the same numerical method over the velocity space for both the second term in the l.h.s. and the r.h.s. of Eq. (4.5) [16, 20]. If we do not integrate the second term of the l.h.s. in the same method as the r.h.s., then the difference between them is comparable with the first term of the l.h.s. $k_\perp^2 A_\parallel$ and numerical instabilities occur.

4.2. Kinetic electrons and adiabatic electrons

Most of the difficulties in the electromagnetic gyrokinetic simulation originate from the large mass ratio between ions and electrons. When the kinetic electrons are included, the mode structure along the magnetic field line is elongated. This is mainly due to the trapped electrons, and thus the elongation is significant for the TEM. In order to capture the elongated mode structure, we need to set the computation domain, $-N_\theta\pi \leqslant z \leqslant N_\theta\pi$, to be very large along the field line $N_\theta \gg 1$, as will be shown in Sec. 6, where z is the coordinate along the magnetic field line, as shown in Sec. 5.1, and N_θ corresponds to N in the equation around Eq. (16) of Ref. [26]. In nonlinear simulations, we normally set $N_\theta = 1$ and set the boundary condition at $z = \pm\pi$ so as to $f(k_x, k_y, z = \pm\pi) = f(k_x + 2\pi\hat{s}k_y, k_y, z = \mp\pi)$ to take into account the magnetic shear. This boundary condition requires a large mode number in the radial direction, because the magnetic shear produces high radial wave number modes. An example is presented in Sec. 8.1.2.

In order to elucidate the kinetic electron effect, here we consider the adiabatic electron approximation. In the large electron thermal velocity limit $v_{Te} \to \infty$ and $\beta_i = 0$ limit, the gyrokinetic equation for electrons Eq. (2.3) is reduced to

$$v_\parallel \mathbf{b}\cdot\nabla\delta f_{e\mathbf{k}_\perp} = v_\parallel \frac{q_e}{T_e} F_{Me}\mathbf{b}\cdot\nabla\phi_{\mathbf{k}_\perp} J_{0e} + \mu\mathbf{b}\cdot\nabla B\frac{\partial\delta f_{e\mathbf{k}_\perp}}{\partial v_\parallel}. \tag{4.6}$$

Since $A_\parallel = 0$ from Ampère's law, the perturbed magnetic field vanishes $\tilde{\mathbf{b}} = 0$, so that $\mathbf{b}^* = \mathbf{b}$. When the mirror term, the second term in the r.h.s. of Eq. (4.6), is neglected, i.e., the trapping of electrons is omitted, we have the adiabatic electron response equation

$$\mathbf{b}\cdot\nabla\delta f_{e\mathbf{k}_\perp} = \frac{q_e}{T_e} F_{Me}\mathbf{b}\cdot\nabla\phi_{\mathbf{k}_\perp} J_{0e}. \tag{4.7}$$

For the analysis of micro-instability in the ion scale, $k_\perp \approx 1/\rho_{Ti} \ll 1/\rho_{Te}$, the electron finite Larmor radius can be neglected, $J_{0e} = 1$ and $\Gamma_{0e} = 1$. Integrating the equation over the velocity space, and then integrating it along the magnetic field line, we have the electron adiabatic response relation

$$\begin{aligned}\delta\hat{n}_{e\mathbf{k}_\perp} &= \frac{-q_e}{T_e}\phi_{\mathbf{k}_\perp} \qquad \text{for} \quad k_y \neq 0, \\ &= \frac{-q_e}{T_e}(\phi_{\mathbf{k}_\perp} - \langle\phi_{\mathbf{k}_\perp}\rangle) \qquad \text{for} \quad k_y = 0,\end{aligned} \tag{4.8}$$

where $\delta\hat{n}_{e\mathbf{k}_\perp} = \int \delta f_{e\mathbf{k}_\perp} d^3v$. Substituting Eq. (4.9) into Eq. (2.4) and neglecting the l.h.s. of Eq. (2.4) because $k_\perp \ll 1/\lambda_{Di}$ for ion scale turbulence, we have a simplified version of Poisson equation Eq. (2.4) for the adiabatic electrons,

$$q_i \int \delta f_{i\mathbf{k}_\perp} J_{0i} d^3v = \frac{q_i^2}{T_i}(1 - \Gamma_{0i})\phi_{\mathbf{k}_\perp} + \frac{q_e^2}{T_e}\phi_{\mathbf{k}_\perp} \quad \text{for} \quad k_y \neq 0, \tag{4.9}$$

$$= \frac{q_i^2}{T_i}(1-\Gamma_{0i})\phi_{\mathbf{k}_\perp} + \frac{q_e^2}{T_e}(\phi_{\mathbf{k}_\perp} - \langle\phi_{\mathbf{k}_\perp}\rangle) \quad \text{for} \quad k_y = 0.$$

The equation can be solved by coupling only with the ion gyrokinetic equation.

We have seen the derivation of the adiabatic electron model by neglecting magnetic perturbation and some dynamics of electrons such as particle trapping. In other words, the neglected dynamics is the typical feature additionally included in the electromagnetic gyrokinetic model extended from the adiabatic electron model. Those are trapped electrons and electron inertia effects as well as the magnetic perturbation. The additional physics causes waves which may limit the time step of numerical simulations, as shown in the next subsection.

4.3. Waves in electromagnetic gyrokinetic system

The time step of numerical simulation Δt can be limited by waves propagating with high frequency. In the electromagnetic gyrokinetic systems we have the kinetic Alfvén wave (KAW) and the high frequency modes in addition to the drift-wave and the sound wave. When $\omega\Delta t$ is too large, this can lead to numerical instabilities for explicit time-integration schemes, where ω is a typical frequency of the waves.

We consider a uniform plasma slab, so that the magnetic drift terms and the mirror term can be neglected in Eq. (2.3). The finite Larmor radius effect is approximated to $\Gamma_{0i} \approx \rho_{Ti}^2 k_\perp^2$ and $\Gamma_{0e} \approx 0$ by assuming $k_\perp \rho_{Ti} \ll 1$. The dispersion relation of waves propagating in the plasma is

$$-\rho_{Ti}^2 k_\perp^2 = \left(\frac{\omega^2}{v_A^2 k_\parallel^2} - 1\right)\left(\sum_s \frac{T_e}{T_s}[1 + \zeta_s Z(\zeta_s)]\right), \tag{4.10}$$

where $Z(\zeta)$ is the plasma dispersion function [46] and $\zeta = \omega/(\sqrt{2}v_{Ts}k_\parallel)$. When $k_\parallel v_{Ti} \ll \omega \ll k_\parallel v_{Te}$, Eq. (4.10) is reduced to the dispersion relation of the kinetic Alfvén wave (Eq. (16) in Ref. [47])

$$\omega^2 = v_A^2 k_\parallel^2 (1 - \rho_{Ti}^2 k_\perp^2). \tag{4.11}$$

On the other hand, when $k_\parallel v_{Te} \ll \omega \ll k_\parallel v_A$ ($\beta_e \ll m_e/m_i$) Eq. (4.10) is reduced to

$$\omega_H^2 = \frac{k_\parallel^2}{k_\perp^2}\Omega_{Ti}^2 \frac{m_i}{m_e}. \tag{4.12}$$

This mode has very high frequencies and restricts the time step of numerical simulations Δt for low $k_\perp$ modes at very low beta $\beta_i \ll m_e/m_i$. It is noticed that this mode remains even in fluid models when we retain the electron inertia, as shown in Appendix D.

5. Setting of numerical simulations

5.1. Flux tube geometry

In order to describe micro-instabilities, it is convenient to use the magnetic field coordinate system, which consists of a coordinate along the magnetic field line and coordinates normal to the field line. Here, we briefly describe the flux tube coordinate $(x, y, z, v_\parallel, \mu)$, where $x = \frac{q(\psi_0)}{B_0 r(\psi_0)}(\psi - \psi_0)$, $y = \frac{-r(\psi_0)}{q(\psi_0)}(\alpha - \alpha_0)$, and $z = \theta$, where $\alpha = \zeta - q(\psi)\theta$ is the magnetic field line label, ψ is the magnetic flux, θ is the poloidal angle, and the tube is located on a field line with $\psi = \psi_0$ and

$\alpha = \alpha_0$ [26], where (ψ, θ, ζ) is a flux coordinate. The parallel gradient along the equilibrium field is written as $\mathbf{b} \cdot \nabla = \frac{1}{q_0 R} \frac{\partial}{\partial z}$ in terms of the magnetic field aligned coordinate z in Eq. (2.3). The periodic boundary conditions are assumed in the poloidal and toroidal directions. The square of the perpendicular wavenumber and the diamagnetic drift frequencies are written as $k_\perp^2 = (k_x + \hat{s} z k_y)^2 + k_y^2$ and

$$\mathbf{v}_{*s} \cdot \mathbf{k}_\perp = k_y \frac{-T_s}{q_s L_n B} \left[1 + \left(\frac{v_\parallel^2}{2} + \mu B - \frac{3}{2} \right) \eta_s \right], \tag{5.1}$$

respectively. The ion and electron temperatures are set to be equal $T_i = T_e$ in the following simulations, so that $\beta_i = \beta_e = \beta/2$. In numerical simulations the Lenard-Bernstein collision operator [34, 48],

$$C_s(h_{s\mathbf{k}_\perp}) = \nu_{ss} \left[\frac{\partial}{\partial v_\parallel} \left(v_\parallel h_{s\mathbf{k}_\perp} + v_{Ts}^2 \frac{\partial h_{s\mathbf{k}_\perp}}{\partial v_\parallel} \right) + \frac{1}{v_\perp} \frac{\partial}{\partial v_\perp} \left(v_\perp^2 h_{s\mathbf{k}_\perp} + v_{Ts}^2 v_\perp \frac{\partial h_{s\mathbf{k}_\perp}}{\partial v_\perp} \right) \right], \tag{5.2}$$

is used, where $h_{s\mathbf{k}_\perp} = \delta f_{s\mathbf{k}_\perp} + \frac{q_s}{T_s} \phi_{\mathbf{k}_\perp} J_{0s} F_{Ms}$ is the non-adiabatic part of the perturbed part of the gyro-center distribution function.

In our numerical simulations, the time integration is made by the fourth-order Runge-Kutta-Gill method, and the z and $v_\parallel$ derivatives are approximated by a finite-difference method.

5.2. Cyclone base case (CBC) tokamak

Calculations are mainly carried out for the Cyclone base case (CBC) tokamak parameters [6]: $q_0 = 1.4$, $\hat{s} = 0.786$, $\eta_i = \eta_e = 3.1$, $R/L_n = 2.22$, $R/L_{Ti} = R/L_{Te} = 6.88$, $\epsilon = r_0/R = 0.18$, $T_i = T_e$, and $m_i/m_e = 1836$, where $\eta_s = L_n/L_{Ts}$. We assume a large aspect ratio tokamak with concentric circular magnetic surfaces. The magnetic field is given by $B = B_0/(1 + \epsilon \cos z)$, and the magnetic drift frequencies are written as

$$\mathbf{v}_{ds} \cdot \mathbf{k}_\perp = \frac{-T_s}{q_s R B} (v_\parallel^2 + \mu B) \left(k_x \sin z + k_y (\cos z + \hat{s} z \sin z) \right). \tag{5.3}$$

Wavenumbers in Fourier space are represented by $k_x = k_{x,min} m$ and $k_y = k_{y,min} k$, where the total number of Fourier modes for k_x and k_y are 288 and 72, respectively, and the minimum wavenumbers are set to $k_{x,min} = 0.031/\rho_{Ti}$ and $k_{y,min} = 0.05/\rho_{Ti}$. In the z, $v_\parallel$, and μ directions, 64, 64, and 16 grid points are distributed in $-\pi \leqslant z \leqslant \pi$, $-4 v_{Ts} \leqslant v_\parallel/v_{Ts} \leqslant 4$, $0 \leqslant \mu B_0/T_s \leqslant 8$, respectively. In order to study turbulence in weakly collisional plasmas, the collision frequency should be sufficiently small, so that it does not influence the growth of instabilities. On the other hand, the collision frequency should be finite in order to obtain a steady state in nonlinear simulations [40], as suggested by Eq. (3.13) and as will be shown in Sec. 7.1. The collision frequencies and the Debye length are set to $\nu_{ii} = 2 \times 10^{-3}$, $\nu_{ee} = \sqrt{m_i/m_e} \nu_{ii}$, and $\lambda_{Di}/\rho_{Ti} = 0$, respectively.

5.3. Helical plasmas

Heliotron/stellarator devices confine plasmas with three-dimensional magnetic fields produced by external coils, and thus are advantageous in maintaining a steady discharge. The importance of the interplay between the ITG turbulence and zonal flows in the Large Helical Device (LHD) [49], which is a heliotron device, was reported by means of electrostatic gyrokinetic simulations with adiabatic electrons

[50], and it is reported that a neoclassical optimization of the magnetic configuration leads to reduction of heat transport through the enhancement of zonal flows. The LHD plasma is normally free from the current driven instability, while the pressure driven instabilities such as ballooning modes can degrade the confinement of plasmas in high-beta discharges [51], and the threshold of KBM is normally lower than that of the ideal MHD ballooning mode [32, 33].

Gyrokinetic simulations of finite beta LHD plasmas are presented here as a typical example of electromagnetic turbulent transport study in three-dimensional systems. The GKV+ code is applied to the analysis of turbulent transport due to micro-instabilities at finite-beta in a model configuration of standard LHD plasmas [50, 52]. The magnetic field strength of the model LHD plasma is given by

$$B = B_0 \left(1 - \epsilon_{00} - \epsilon_t \cos z - \sum_{l=L-1}^{l=L+1} \epsilon_l \cos[(l - Mq_0)z - M\alpha] \right), \tag{5.4}$$

in terms of the flux tube coordinate $(x, y, z, v_\parallel, \mu)$ [26], and the magnetic drift frequency is given by

$$\mathbf{v}_{ds} \cdot \mathbf{k}_\perp = \frac{-1}{q_s B}(v_\parallel^2 + \mu B)\frac{\epsilon_t}{r} \left[k_y \left(\frac{r\epsilon_{00}'}{\epsilon_t} + \frac{r\epsilon_t'}{\epsilon_t} \cos z + \sum_{l=L-1}^{l=L+1} \frac{r\epsilon_l'}{\epsilon_t} \cos[(l - Mq_0)z - M\alpha] \right) \right.$$
$$\left. + (k_x + \hat{s} z k_y) \left(\sin z + \sum_{l=L-1}^{l=L+1} l \frac{\epsilon_l}{\epsilon_t} \sin[(l - Mq_0)z - M\alpha] \right) \right] \tag{5.5}$$

where $\hat{s} = \frac{r}{q}\frac{dq}{dr}$ and $\epsilon' = a\frac{d\epsilon}{dr}$, $L = 2$, $M = 10$, and $\alpha = 0$. Other parameters for the standard LHD configuration are $q_0 = 1.9$, $\hat{s} = -0.85$, $\eta_i = \eta_e = 3$, $R/L_n = 3.33$, $R/L_T = 10$, $T_i = T_e$, $\epsilon_{00} = 0$, $\epsilon_t = 0.087$, and $(\epsilon_{L-1}, \epsilon_L, \epsilon_{L+1}) = \epsilon_t(-0.28, 0.91, 0)$. Turbulent transport due to the KBM at $\beta_i = 1.7\%$ is investigated and is compared with the ITG turbulence at $\beta_i = 0.2\%$. In the simulations, the number of Fourier modes is $(144, \pm 36)$ with $(k_{x,min}\rho_{Ti}, k_{y,min}\rho_{Ti}) = (0.077, 0.058)$ for KBM and $(k_{x,min}\rho_{Ti}, k_{y,min}\rho_{Ti}) = (0.12, 0.046)$ for ITG, and 256, 64, and 32 grid points are distributed in the z, $v_\parallel$, and μ direction, respectively. The resolution in the radial direction is required to capture an elongated mode structure along the magnetic field line by taking into account the magnetic shear that causes high-radial wavenumber Fourier modes. The resolution in the velocity space is required to reduce numerical error, so that numerical solutions satisfy the entropy balance equation Eq. (3.1). The collisions between ions and electrons are neglected, and the collision frequency and the Debye length are set to be $\nu_{ii} = 2 \times 10^{-3}$, $\nu_{ee} = \sqrt{m_i/m_e}\nu_{ii}$, and $\lambda_{Di}/\rho_{Ti} = 0$, respectively.

6. Micro-instabilities in finite beta plasmas

6.1. Tokamak (Cyclone base case)

6.1.1. Ballooning parity modes In this linear analysis plasmas are assumed to be collisionless $\nu_{ss} = 0$. Growth rates and real frequencies for $k_y\rho_{Ti} = 0.2$ mode are plotted as a function of β_i in Fig. 2. The ion temperature gradient (ITG) mode is unstable at low beta, and its real frequency ω is negative, which implies that the ITG mode rotates toward the ion diamagnetic direction on a cross section of the torus. The growth rate of ITG instability decreases with β_i up to $\beta_i = 0.9\%$, while

the absolute value of real frequency increases slightly. When β_i is around 1%, the trapped electron mode (TEM) is unstable. The TEM has positive real frequency and rotates toward the electron diamagnetic direction. The growth rate of TEM is smaller than that of the ITG mode at the low wavenumber $k_y\rho_{Ti} = 0.2$. When β_i is above 1.3%, the kinetic ballooning mode (KBM) is unstable. The real frequency of KBM is negative and its absolute value is larger than that of the ITG mode. The rotation direction of KBM is in the ion diamagnetic direction and is the same as that of the ITG mode. The growth rate of KBM increases with β, while its absolute value of real frequency decreases. The growth rate and real frequency obtained here are similar to those in the previous work [12, 18, 19]. The dependence of instability on plasma beta is strong for ion scale micro-instabilities $k_y\rho_{Ti} < 1$, i.e., the ITGs are unstable at low beta and KBMs are unstable at high beta [15, 28]. On the other hand, the growth rates of instabilities for $k_y\rho_{Ti} \geqslant 1$ such as TEM/ETG mode are not influenced by the value of plasma beta.

Figure 3 shows the growth rate as a function of the poloidal wavenumber k_y for $\beta_i = 0.2\%$, 1.0%, and 1.4%. The TEMs around $k_y\rho_{Ti} \approx 0.8$ are not influenced by the increase of the beta value. On the other hand, the ITG mode, which is unstable for $k_y\rho_{Ti} < 0.5$ at $\beta_i = 0.2\%$, almost disappears at $\beta_i = 1.\%$ and 1.4%, while KBM is unstable $k_y\rho_{Ti} < 0.5$ at $\beta_i = 1.4\%$. The TEMs are unstable for all wavenumbers at $\beta_i = 1.\%$. The wavenumber of the most unstable KBM is smaller than that of the ITG mode.

Figure 4 shows the profile of the electrostatic potential with the wavenumber $k_y\rho_{Ti} = 0.2$, 0.3, and 1.0 along the magnetic field line z. The perturbations of ITG, TEM, and KBM have a peak at $z = 0$, which is the out side of the torus and is called the bad curvature region. Since the ITG mode is a ballooning type instability, a sharply peaked mode at the bad curvature region has a larger growth rate than a broadened mode. In fact, the ITG with $k_y\rho_{Ti} = 0.3$ is more unstable and sharply peaked than that with $k_y\rho_{Ti} = 0.2$, as shown in Figs. 3 and 4. These profiles imply that ITG mode, TEM, and KBM have a ballooning structure localized at $z = 0$ and have the ballooning parity (see Sec. 3.3). The profiles of ITG mode, TEM, and KBM with $k_y\rho_{Ti} = 0.2$ and 0.3 extend over $z = \pm 2\pi$. On the other hand, the profiles of TEM with $k_y\rho_{Ti} = 1.0$ extends over $\pm 8\pi$, and the profiles are not influenced by beta value. This very elongated mode structure along the field line is a typical feature of TEMs. It is remarked that the electrostatic potential ϕ has the same parity as the distribution function while the parallel component of the vector potential $A_\parallel$ has the opposite parity. Figure 5 shows the profile of the parallel component of the vector potential along the magnetic field line z for the ITG mode with $k_y\rho_{Ti} = 0.2$, TEM with $k_y\rho_{Ti} = 1.0$, and MTM with $k_y\rho_{Ti} = 0.09$. The ITG mode and TEM are an odd function against z, so that they are classified into the ballooning parity modes (See Table 1).

6.1.2. Tearing parity modes A typical tearing parity instability is the micro-tearing mode (MTM) [53, 54, 55, 56, 57]. In order to investigate MTM, we consider a large beta tokamak plasma such as a spherical tokamak. The MTM is normally destabilized by the electron temperature gradient and by the electron-ion collisions. Since the electron-ion collision operator is not implemented in our code, a large electron-electron collision frequency $\nu_{ee} = 0.16$ is used in this analysis instead. Other parameters, which are different from CBC, are $\beta_i = 6\%$ and $1/L_{Ti} = 0$. The growth rate and real frequency of $k_y\rho_{Ti} = 0.09$ mode are $\gamma = 0.19$ and $\omega = 2.v_{Ti}/R_0$, respec-

tively. The positive real frequency indicates that the MTM rotates in the electron diamagnetic direction. The electrostatic potential is an odd function against the coordinate along the magnetic field line z, while the vector potential is an even function, as shown in Figs. 4 and 5, and thus this mode is classified into the tearing parity mode (Table 1).

6.2. Helical plasma

The beta dependence of the instability in helical plasmas is similar to that in the CBC tokamak plasma, as shown in Fig. 6 [35, 42, 58]. The ITG mode is unstable for $\beta_i < 1\%$ and the KBM is unstable for $\beta_i > 1.3\%$. The TEM does not appear around $\beta_i = 1.2\%$ which is located between ITG mode unstable and KBM unstable regimes. The significant difference from the tokamak plasma is that the most unstable KBM has a finite ballooning angle $\theta_k = -k_x/(k_y\hat{s}) \neq 0$ ($k_x \neq 0$) and an inclined mode structure with respect to the mid-plane of a torus. The profile of the perturbation on xy-plane at $z = 0$ is inclined because of the finite radial wavenumber (Fig. 7). This is in contrast to KBMs in tokamaks as well as ITG modes in tokamaks and helical systems. Figure 8 shows the profile of the electrostatic potential ϕ and the parallel component of vector potential $A_\parallel$ of the most unstable ITG mode with $\mathbf{k}_\perp = (0, 0.3/\rho_{Ti})$ at $\beta_i = 0.2\%$ and of the most unstable KBM with $\mathbf{k}_\perp = (0.2/\rho_{Ti}, 0.3/\rho_{Ti})$ at $\beta_i = 2\%$ along the magnetic field line z for LHD with $\eta_e = 0$. The electrostatic potential of ITG for $\beta_i = 0.2\%$ has a peak at $z = 0$ and has an oscillation due to the particle trapped by helical ripples. The electrostatic potential is an even function of z and the vector potential is an odd function of z, and thus the mode is classified into the ballooning parity mode. On the other hand, the potential of the KBM for $\beta_i = 2\%$ has a peak at $z \approx \pi/4$, i.e., the mode has a finite ballooning angle $\theta_k \approx \pi/4$. The finite ballooning angle appears when particle trapping at helical ripples is significant because the bounce average of magnetic drift velocity Eq. (5.5) has a finite radial component to destabilize the Fourier modes with finite radial wavenumber. This inclined mode structure is the origin of the saturation of KBM turbulence in helical plasmas, as shown in Sec. 8.2.

7. Microturbulence at finite beta (Nonlinear simulations)

7.1. Beta dependence of turbulent transport

Nonlinear simulation results for several beta values are presented in this section [18, 19, 21, 22]. It is to be noted that the magnetic field configuration and temperature and density profiles are fixed and the value of β_i in the Ampère's law Eq. (2.5) is changed. Figure 9 shows the electrostatic potential profile in the configuration space. During the growing phase (Fig. 9 (a)), the perturbed potential for $\beta_i = 0.2\%$ exhibits a clear ballooning structure of the ITG mode and TEM, which are strong (weak) and elongated in the radial (poloidal) direction around the outside (inside) of the torus. The alternative stripes of bright and dark are following along the magnetic field line on the surface of the torus in Fig. 9, while a fine structure appears on a cross section of the torus. The structure indicates that the turbulence has a flute structure $k_\parallel \ll k_\perp$, as described in Sec. 2. Figure 9 (b) shows the potential profile in a statistically steady state for $\beta_i = 0.2\%$. The profile shows that zonal flows appear and regulate the ITG/TEM turbulence. As the beta is increased to $\beta_i = 0.4\%$ and 0.6% (Fig. 9 (b) and (c)), the zonal flows become stronger than the turbulence in the steady state, and thus the heat transport is reduced compared

with that for $\beta_i = 0.2\%$, as shown below. For $\beta_i = 0.8\%$ the turbulence continues to grow with a long wavelength perturbation that is stronger than the zonal flows in the nonlinear evolution, and the heat transport continues to grow correspondingly.

Figure 10 (a) shows the β dependence of turbulent energy transport coefficient $\chi_s = Q_s L_{Ts}$. The energy flux is $Q_s = \Theta_s + \frac{5}{2} T_s \Gamma_s$, where, $\Theta_s = \Theta_{es,s} + \Theta_{em,s}$ and the ion heat flux due to electrostatic potential perturbation is denoted by $\Theta_{es,ion}$, for instance, as defined in Sec. 3.1. The transport is caused by the ITG turbulence and decreases as ion beta β_i increases from 0.2% to 0.6%, because the linear growth rate of the ITG mode is reduced with β_i, while the zonal flow is not so influenced by the increase of beta, as will be shown by the zonal component ($k_y = 0$) of electrostatic potential spectrum in Fig. 11. The electron energy transport in Fig. 10 (a) is not so affected by the increase of beta. It is noticed that the energy transport increases to a very large value when β_i exceeds 0.8%. This will be discussed in Sec. 7.3.

Figure 10 (b) shows the contribution of electrostatic potential and magnetic perturbation to the energy transport presented in Fig. 10 (a). The ion energy transport is dominantly caused by the electrostatic perturbation, while the contribution of magnetic perturbation to the ion heat transport is very small and negative, i.e., it has very small pinch effect. In contrast with the ion transport, the electron energy transport is significantly influenced by the magnetic perturbation. The contribution of the magnetic perturbation is small at $\beta_i = 0.2\%$ because of the small magnetic perturbation as expected from the Ampère's law Eq. (2.5). The contribution increases with beta and becomes the same order as that of the electrostatic perturbation at $\beta_i = 0.6\%$. Since the contribution from the electrostatic perturbation is decreased with beta, the electron energy transport almost does not depend on beta from $\beta_i = 0.2\%$ to 0.6%. The magnetic part becomes comparable with the electrostatic part for $\beta_i \geqslant 0.8\%$ and is very large. This large contribution of magnetic perturbation may be linked to the very large value of the transport for $\beta_i \geqslant 0.8\%$ through the zonal flow production, as will be discussed in Sec. 7.3.

Figure 11 shows the electrostatic potential spectra averaged from $t = 50$ to $t = 180$. Each spectrum has a peak around $k_y \rho_{Ti} = 0.2$ for $\beta_i \leqslant 0.6\%$, and the ITG mode around $k_y \rho_{Ti} = 0.2$ dominantly contributes the energy transport, in spite of the fact that the linear growth rate of TEM at $k_y \rho_{Ti} \approx 1$ is higher than that of the ITG mode. The other peak of the spectrum is located at $k_y = 0$, which is the zonal component. The zonal flows regulate the ITG and TEM turbulence, and the strength of the flow is not so affected by the increase of beta up to $\beta_i \leqslant 0.6\%$, so that the amplitude of the ITG turbulence is decreased with beta because of the decrease of the linear growth rate. On the other hand, the zonal flows become weak for $\beta_i = 0.8\%$, and, correspondingly, the amplitude of ITG turbulence becomes large, so that the energy transport is very large, as shown in Fig. 10.

The comparison of Fig. 10 with Fig. 2 implies that the heat flux decreases with β faster than the linear growth rate. The linear growth rate at $\beta_i = 0.6\%$ is 3/4 of the $\beta_i = 0.2\%$ case. On the other hand, the heat flux at $\beta_i = 0.6\%$ is one-half of that at $\beta_i = 0.2\%$. One of the reasons is the beta dependence of zonal flow production [19]. The zonal flow shearing decreases with beta slower than the linear growth rate. Thus, the decrease of the linear growth rate plus the slower decrease of zonal flow production with beta may explain the faster decrease of the ion heat flux with beta compared to the electron heat flux in Fig. 10. The Dimits shift is suggested by the fact that the zonal flows play an essential role at low beta ITG turbulence.

Although it is not confirmed by our own simulation, it is reported that the shift is enhanced by the finite beta effects and increases with beta up to 30% [21].

7.2. Entropy transfer

Here we investigate the saturation mechanism of turbulence based on the conserved quantity introduced in Sec. 3.1. Figure 12 (a) shows the time evolution of each term in the entropy balance equation Eq. (3.1) for the ITG turbulence with $\beta_i = 0.2\%$. At the beginning, the ITG mode grows, and the entropy production due to turbulent transport term for ions $\Theta_i/L_{Ti} + \Gamma_i T_i/L_{pi}$ increases and is dominant until $t \approx 20$, and the transport term almost balances with the time derivative of the entropy variable $d\delta S_i/dt$. The increase of $d\delta S_s/dt$ term implies that a fine structure of the distribution function is produced in the velocity space. After $t \approx 50$ the ITG turbulence is saturated and a statistical steady state is established. In the steady state the time derivative terms are very small $\frac{d}{dt}(\sum_s \delta S_s + W_{es} + W_{em}) \approx 0$, and the entropy production due to turbulent transport terms balance with the collisional dissipation terms as shown by Eq. (3.13). The ion (electron) transport term $\Theta_i/L_{Ti} + \Gamma_i T_i/L_{pi}$ ($\Theta_e/L_{Te} + \Gamma_e T_e/L_{pe}$) almost balances with the ion (electron) collisional dissipation term D_i (D_e), however, the balance between them is not complete, and the free energy is transformed from ions to electrons, i.e., $R_i < 0$ and $R_e > 0$, in Eq. (3.12), as shown in Fig. 12 (b). The entropy balance error Δ is much smaller than the entropy production term (free energy term) of ions, and thus the entropy balance equation Eq. (3.1) is well satisfied in the simulation.

Next we consider the spectrum of each term in the entropy balance equation for a Fourier mode $\mathbf{k}_\perp$ in the statistical steady state of the ITG turbulence at $\beta_i = 0.2\%$. Figure 13 shows the spectrum of each term (a) $\mathcal{T}_{s,k_y} = \sum_{k_x} \mathcal{T}_{s\mathbf{k}_\perp}$ as a function of the poloidal wavenumber k_y and (b) $\mathcal{T}_{s,k_x} = \sum_{k_y} \mathcal{T}_{s\mathbf{k}_\perp}$ as a function of the radial wavenumber k_x. Figure 13 (a) shows typical features of the entropy (free energy) transfer in the Fourier mode space. The entropy production due to the ion turbulent transport $\Theta_{i,k_y}/L_{Ti} + \Gamma_{i,k_y} T_i/L_{pi} = \sum_{k_x} \Theta_{i\mathbf{k}_\perp}/L_{Ti} + \Gamma_{i\mathbf{k}_\perp} T_i/L_{pi}$ (red line) is positive and has a peak at $k_y\rho_{Ti} = 0.2$. This means that the ITG instability with $k_y\rho_{Ti} \approx 0.2$ drives the entropy (free energy) of turbulence. The nonlinear entropy transfer spectrum $\mathcal{T}_{s,k_y}$ (blue line) is negative around $k_y\rho_{Ti} = 0.2$ and cancel out $\Theta_{i,k_y}/L_{Ti} + \Gamma_{i,k_y} T_i/L_{pi}$, and it is positive at $k_y\rho_{Ti} < 0.1$ and $k_y\rho_{Ti} > 0.4$. These imply that the entropy produced by the ITG mode is transferred from the ITG unstable region $k_y\rho_{Ti} \approx 0.2$ to the stable high wavenumber region in $k_y\rho_{Ti} > 0.4$ as well as the low wavenumber region including the zonal mode by the nonlinear mode coupling. It is noticed that the zonal component which is the $k_y = 0$ mode does not cause the transport $\Theta_{i,k_y=0}/L_{Ti} + \Gamma_{i,k_y=0} T_i/L_{pi} = 0$ as shown by Eqs. 3.6 and 3.7, so that $\sum_s \left(\mathcal{T}_{s,k_y=0} + D_{s,k_y=0}\right) = 0$ for the zonal component. It is also noticed that $\sum_{k_y} \mathcal{T}_{s,k_y} = \sum_{\mathbf{k}_\perp} \mathcal{T}_{s,\mathbf{k}_\perp} = 0$. The ion collisional dissipation term D_{i,k_y} is negative and balances with the nonlinear entropy transfer term $\mathcal{T}_{i,k_y}$ at high wavenumber. This implies that the transferred entropy is dissipated by the collision at high wavenumber. Furthermore, the collisional dissipation is negative at low wavenumber, so that the nonlinearly transferred free energy to the low wavenumber is also dissipated by the collision. The collisional dissipation plays the significant role at low wavenumber as well as at high wavenumber, because the dissipation occurs not in the configuration space but in the velocity space, as shown by Eq. (5.2). The entropy production, nonlinear entropy transfer, and collisional

dissipation for electrons are similar to those of the ions, except that the amplitudes are almost one-thirds smaller those of the ions.

Figure 13 (b) shows the spectrum of each term as a function of the radial wavenumber k_x. The profiles for $k_x\rho_{Ti} \geqslant 0.05$ are similar to those for $k_y\rho_{Ti} \geqslant 0.2$ in Fig. 13 (a), i.e., the entropy production is strong at $k_x\rho_{Ti} \approx 0.05$, the entropy is transferred to the high wavenumber $k_x\rho_{Ti} > 0.5$ by the nonlinear mode coupling, and it is dissipated by collisions at the high wavenumber $k_x\rho_{Ti} > 0.5$. The profiles at low wavenumber $k_x\rho_{Ti} < 0.05$ are significantly different from those for $k_y\rho_{Ti} < 0.2$ in Fig. 13 (a). This is because the $k_y = 0$ mode represents the zonal component and the entropy can be transferred to the zonal component, while there are no corresponding modes in low k_x region.

Figure 14 shows the spectrum of each term on the $\mathbf{k}_\perp = (k_x, k_y)$ plane. The entropy production term $\Theta_{s\mathbf{k}_\perp}/L_{Ts} + \Gamma_{s\mathbf{k}_\perp} T_s/L_{ps}$ has a peak at $(k_x, k_y) \approx (0.05, 0.2)$, and thus the dominant ITG mode producing entropy has a finite radial wavenumber. This is because the ITG mode is sheared by the zonal flow which has a radial wavenumber. The positive region (denoted by red) of $\Theta_{s\mathbf{k}_\perp}/L_{Ts} + \Gamma_{s\mathbf{k}_\perp} T_s/L_{ps}$ corresponds to the negative region (denoted by blue) of $\mathcal{T}_{s\mathbf{k}_\perp}$ that implies the produced entropy is transferred by the nonlinear mode coupling. The entropy is transferred to high k_x and k_y region, and is also transferred to $k_y \approx 0$ region to produce the zonal component. The transferred entropy is dissipated by the collision $D_{i\mathbf{k}_\perp}$, which is large negative around $k_y \approx 0$, and also negative entire (k_x, k_y) space. The entropy transfer process is significantly anisotropic in (k_x, k_y) space.

The summary of the entropy transfer in ITG turbulence, which is significantly anisotropic, is as follows. The entropy is produced by the ITG mode, and it is transferred not only to the high wavenumber regime but also to the low wavenumber regime including zonal component, and eventually dissipated by the collision in high and low wavenumber regions, as schematically shown in Fig. 15 (a). The picture is significantly different from the energy transfer of the neutral fluid turbulence shown in Fig. 15 (b) (see Fig. 8.10 in Ref. [59] and Fig. 6.5 in Ref. [60]). In the neutral fluid, turbulence is normally driven at low wavenumber as indicated by the red line, and the nonlinear transfer function has the same absolute value at the similar wavenumber and is negative as indicated by the blue line. The transfer function is positive only at the high wavenumber region and it balances with the viscous dissipation represented by the green line. The transfer function is very small between the driven and dissipation regions. This region is called the inertial range, and a scaling of the energy spectrum $E_k \propto k^{-\alpha}$ is expected in this regime. In the ITG turbulence, there is no region where $\mathcal{T}_{sk}$ is zero in Fig. 13, and thus there is no inertial range in the ITG turbulence.

7.3. Saturation problem of turbulence at finite beta

The saturation problem arises in electromagnetic gyrokinetic simulations at finite beta. In Fig. 10 (a) the level of the energy transport for ions and electrons χ_i and χ_e are not at a physically relevant level for $\beta_i = 0.8\%$ and 1%. The saturation problem is called "run-away" in Ref. [22] and is called "non-zonal transition" in Ref. [24]. The heat diffusion coefficient χ_i decreases with plasma beta because of the reduction of the linear growth rate of the ITG mode. However, the transport reaches a very high level when the beta is larger than a critical value $\beta_i = 0.8\%$ in Fig. 10 (a). The linear analysis shows that the instabilities driving turbulence are the ITG mode and TEM at the critical beta of the run-away, and thus the

run-away occurs at a beta that is lower than the threshold of KBM, which appears for $\beta_i > 1.2\%$. Figure 16 shows the time history of the energy diffusivity coefficient for several values of β_i. The growth of ITG/TEM is saturated at a reasonable level at the first saturation at $t = 50$ for each β_i, and the level is roughly proportional to the linear growth rate shown in Fig. 2. The energy transport reaches a statistically steady state for $\beta_i < 0.8\%$ and fluctuates around the averaged saturation level. On the other hand, the transport for $\beta_i \geqslant 0.8\%$ starts to grow again and continues to grow after the first saturation. In particular, it becomes larger than 50 $[v_{Ti}\rho_{Ti}^2/R_0]$ at $t = 90$ for $\beta_i = 1\%$, and eventually the transport reaches thousands in the Gyro-Bohm unit. In this case, zonal flows are weak compared with the amplitude of microturbulence, as shown in Fig. 11 (a). This is the significant difference from the ITG turbulence at very low beta $\beta_i \leqslant 0.6\%$, and the run-away can be linked to the weak zonal flows. The run-away may be also related to the fixed gradient in the local simulations, and thus a saturation of turbulence can be realized at a physically relevant level in finite beta, when a global relaxation of the temperature and density profiles are allowed.

Some possible explanations of the run-away are proposed by Refs. [22] and [24]. One is a sub-critical instability due to the production of a zonal pressure field. When the largest gradient of corrugated pressure profile including the zonal pressure exceeds the critical pressure gradient of the ideal MHD stability, a secondary instability (sub-critical instability) occurs and the heat transport runs away [22]. Another mechanism of the run-away is the production of a stochastic magnetic field. The effects of magnetic perturbation on the transport becomes significant for $\beta_i \geqslant 0.8\%$, as shown in Fig. 10 (b). This implies that the large magnetic perturbation may play a role in the run-away. The stochastic field may prevent the formation of zonal flows [24, 29].

7.4. Impact of magnetic perturbation on turbulent transport

The influence of magnetic perturbation on the turbulent transport is reported here. The effect is called magnetic flutter and it is caused by the perturbed part of the parallel gradient of the perturbation. The effect is written in terms of the Poisson bracket $(\tilde{\mathbf{b}}\cdot\nabla f)_{\mathbf{k}_\perp} = -[A_\parallel J_{0s}, f]_{\mathbf{k}_\perp}$ in Eq. (2.3). In the ITG/TEM turbulence at low beta, the impact of magnetic flutter on the ion energy transport is typically small compared with that of the E×B flow convection due to the electrostatic potential perturbation, as shown in Fig. 10 (b). On the other hand, the contribution of the magnetic flutter on the electron heat transport is comparable with that of the E×B flow convection at finite beta in Fig. 10 (b). It is reported that the transport due to the magnetic flutter is proportional to the square of beta β^2 in ITG turbulence [19], and that is explained by the production of a stochastic magnetic field. The violation of magnetic surface is caused by the production of the tearing parity, as explained in Sec. 3.3. The magnetic perturbation that has tearing parity is produced by the ITG mode through the parity exchange caused by the nonlinear term Eq. (3.24).

Turbulence driven by the micro-tearing mode (MTM) is significantly different from the ITG turbulence at low beta because the MTM is essentially electromagnetic instability. As we have discussed in Sec. 3.3, the parallel component of vector potential $A_\parallel$ of MTM is an even function against the coordinate along the magnetic field line z, so that the violation of the magnetic surface causes the instability. Although we have not confirmed by our own simulation, it is reported that the heat flux due to the magnetic perturbation is well explained by the Rechester-Rosenbluth

model, but the model breaks down when the amplitude of the magnetic perturbation is small [55].

7.5. Interaction between ITG and ETG

The electromagnetic microturbulence described above is in the ion scale $k_\perp \approx 1/\rho_{Ti}$, while there is microturbulence in the electron scale $k_\perp \approx 1/\rho_{Te}$. In fact, the TEM connects to the electron temperature gradient (ETG) mode at high wavenumber region in Fig. 3. One of the examples of high performance computing is a simulation covering both ion and electron scales. The simulation enables us to understand the interaction between ITG turbulence and ETG turbulence. Although the growth rate of ETG mode is much larger than that of ITG mode, the ion scale turbulence, which is regulated by zonal flows, dominates and controls the turbulent heat transport of ions and electrons in a statistically steady state [61, 62].

8. Saturation of KBM turbulence with small electron temperature gradient

The subject of this section is the identification of a saturation mechanism for finite beta microturbulence in regimes where zonal flow production is weak [35, 42, 39, 63].

8.1. CBC

8.1.1. Saturation of KBM turbulence We have a saturation of the growth of KBM when the electron temperature gradient is set to be small [35, 39]. The growth of the electron temperature gradient (ETG) mode is avoided by setting the electron temperature gradient to be small $\eta_e = 0$ or 0.2 in the simulations. Figure 17 shows the linear growth rate of KBMs with $\beta_i = 2.\%$ as a function of k_y for $\eta_e = 0$ and 0.2. The growth rate of the most unstable mode for $\eta_e = 0.2$ is larger than that for $\eta_e = 0$. The growth rate is negative for $k_y\rho_i > 1$, because the KBMs are stabilized by the finite ion Larmor radius effects and the ETG is stabilized by choosing small η_e. Figure 18 shows the time history of each term in the entropy balance equation for $\beta_i = 2.\%$ and $\eta_e = 0.2$. The KBM turbulence reaches a statistically steady state with a physically relevant level of transport, $\Theta_i = 2.9T_i v_{Ti}\rho_{Ti}^2/L_n^2$, $\Theta_e = 0.32T_i v_{Ti}\rho_{Ti}^2/L_n^2$, $\Gamma = 0.71 n_0 v_{Ti}\rho_{Ti}^2/L_n^2$. Figure 19 shows the spectrum of the electrostatic potential in the steady state. It has a sharp peak of KBM at $k_y\rho_{Ti} = 0.2$, and the zonal component $k_y\rho_{Ti} = 0$ is much smaller than the dominant KBM. Hence, there are some cases which are free from the saturation problem, when η_e is small, even when the zonal flows are weak.

8.1.2. Saturation caused by extended mode structure along the field line(Entropy transfer) In order to identify the saturation mechanism of turbulence it is useful to examine nonlinear Fourier mode coupling by evaluating the entropy transfer function Eq. (3.16). Here, we study the saturation of KBMs in CBC with $\eta_e = 0$ and $\beta_i = 2\%$ presented in the previous subsection [35]. The dominant KBM in the steady state is $\mathbf{k}_\perp = (k_x\rho_{Ti}, k_y\rho_{Ti}) = (0, 0.2)$, as shown in Fig. 19. We study the saturation of this mode by evaluating the entropy transfer function around $t = 50L_n/v_{Ti}$. Figure 20 (a) shows the nonlinear entropy transfer function averaged from $t = 50$ to $60L_n/v_{Ti}$ in the saturation phase. The transfer function is negative, which is represented by blue region, at $\mathbf{k}'_\perp = (k'_x\rho_{Ti}, k'_y\rho_{Ti}) = (1, 0.2)$ and (1,0). This implies that the saturation of $(0, 0.2)$ mode is caused by the nonlinear Fourier

mode interaction with $(1, 0.2)$ and zonal mode $(1, 0)$. This interaction is visible in Fig. 22 (Fig. 4 of Ref. [35]) showing that $(k_x\rho_{Ti}, k_y\rho_{Ti}) = (0, 0.2)$ mode interacts with $(1., 0.2)$ mode represented by the fine vertical stripe structure of perturbation on the $z = 0$ plane. The transfer function of zonal mode $(k_x\rho_{Ti}, k_y\rho_{Ti}) = (0, 1)$ shows that $(k'_x\rho_{Ti}, k'_y\rho_{Ti}) = (1, 0.2)$ and $(0, 0.2)$ are large positive in Fig. 20 (b), thus the entropy or free energy is transformed from the KBM with $(0, 0.2)$ and $(1, 0.2)$ to the zonal mode with $(0, 1)$. It is noticed that $\mathbf{k}'_\perp$ satisfies $\mathbf{k}'_\perp = \mathbf{k}_\perp - \mathbf{k}''_\perp$ (see Eq. (3.17)). Figure 21 shows this transfer schematically in terms of the diagram introduced in Fig. 1.

Here, we discuss the mode $\mathbf{k}_\perp = (k_x\rho_{Ti}, k_y\rho_{Ti}) = (1, 0.2)$ that is responsible for the saturation of the KBM with $\mathbf{k}_\perp = (0, 0.2)$. The mode structure of KBM along the field line extends wider than $\pm\pi$, as shown in Fig. 23 (a). The $(1, 0.2)$ mode is, in fact, connected to $(0, 0.2)$ mode at $z = \pm\pi$. In the flux tube model we can describe perturbation extending beyond $\pm\pi$ by connecting other Fourier modes through the boundary conditions by taking into account the magnetic shear from (k_x, k_y) to $(k_x + 2\pi\hat{s}k_y, k_y)$ when the simulation domain is in $-\pi \leqslant z \leqslant \pi$, where $\hat{s}$ is the magnetic shear [26]. In this simulation $(k_x\rho_{Ti}, k_y\rho_{Ti}) = (0, 0.2)$ mode is connected to $(1., 0.2)$ mode at $z = \pm\pi$, as shown in Fig. 23 (a). When we solve a linearized equation in the flux tube geometry, a calculation for $(k_x\rho_{Ti}, k_y\rho_{Ti}) = (0, 0.2)$ with $(k_x\rho_{Ti}, k_y\rho_{Ti}) = (1, 0.2)$ in $[-\pi : \pi]$ is exactly the same as the calculation of $(k_x\rho_{Ti}, k_y\rho_{Ti}) = (0, 0.2)$ in the simulation box $[-2\pi : 2\pi]$. However, in nonlinear evolution, the $(1, 0.2)$ mode can interact with the $(0, 0.2)$ mode through nonlinear Fourier mode coupling. In fact, this interaction causes the saturation of the growth of $(0, 0.2)$ KBM as described by the diagram in Fig. 21. Hence, the KBM becomes saturated by the interaction with the mode caused by the elongated mode structure along the magnetic field line in this simulation. It is noticed that the saturation mechanism described here plays a role in the ITG/TEM turbulence in Sec. 7.1, however, the stabilizing effects by zonal flow shear is much stronger than the interaction caused by the elongated mode structure, and thus the mechanism is not responsible when zonal flows are strong.

8.1.3. Higher saturation level with elongated flux tube It is shown that the KBM is saturated by the interaction with the mode produced by the extended structure of fluctuation along the magnetic field line in the previous subsection. The interaction can be avoided by extending the simulation box along the field line, i.e., in z-direction, from $[-\pi : \pi]$ to $[-N_\theta\pi : N_\theta\pi]$ with an integer N_θ [26]. Figure 23 (b) shows that the KBM with $(k_x\rho_{Ti}, k_y\rho_{Ti}) = (0, 0.2)$ and the other KBM $(k_x\rho_{Ti}, k_y\rho_{Ti}) = (1, 0.2)$ are not connected at $z = \pm\pi$, and thus these two modes are independent during their linear growth. Since these two KBMs are independent during the linear growth phase, their nonlinear mode coupling can be reduced.

Figure 24 shows the time history of heat flux with $N_\theta = 1$ and $N_\theta = 2$. For $\beta = 2\%$ the ion heat flux Θ_{ion} with $N_\theta = 1$ reaches a steady state around $t = 40L_n/v_{Ti}$ and is about 2 $T_i v_{Ti}\rho_i^2/L_n^2$ in the steady state (Fig. 24 (a)). The heat flux with $N_\theta = 2$ starts to become saturated around $t = 40$, then continues to grow. The heat flux increases more than 1000 times of that with $N_\theta = 1$, and a steady state is not obtained. Figures 24 (b) shows the time history of ion heat flux for 1.8%. The KBM turbulence in the extended domain simulations with $N_\theta = 2$ is saturated and reaches a statistical steady state. Their amplitudes are much larger than that from the calculation with $N_\theta = 1$. Hence, the interaction of the KBM with the

connected mode, which is shown in the diagram (Fig. 21), is significantly reduced in the calculation with $-2\pi \leqslant z \leqslant 2\pi$ ($N_\theta = 2$), and the level of turbulent transport with $-2\pi \leqslant z \leqslant 2\pi$ is much higher than that with $-\pi \leqslant z \leqslant \pi$ ($N_\theta = 1$).

8.2. Electromagnetic turbulence in three-dimensional magnetic field

Saturation of turbulent transport in finite-beta helical plasmas is reported here. A statistical steady state of the KBM turbulence at high beta is obtained and compared with that of the ITG turbulence for a model configuration of standard LHD plasma. The most unstable KBM in LHD has a finite radial wavenumber and a finite ballooning angle as shown in Figs. 6 and 8. The perturbation of the KBM is inclined on the xy plane because of the finite radial wavenumber, as shown in Fig. 7. In nonlinear simulations two oppositely inclined KBMs grow. One has a positive radial wavenumber and the other has a negative wavenumber. The simulation reveals that the growth of KBM in LHD is saturated by nonlinear interactions of oppositely inclined convection cells, which are peaked at finite z, through mutual shearing (Fig. 25 (b) and Fig. 26 with the title "KBM"). The saturation mechanism is in contrast with that of the ITG turbulence regulated by zonal flows (Fig. 25 (a) and Fig. 26 with the title "ITG").

The saturation mechanism is quantitatively investigated by evaluating the nonlinear entropy transfer function $T(\mathbf{k}_\perp; \mathbf{k}'_\perp, \mathbf{k}''_\perp)$ of triad Fourier mode interaction [42]. There are two main directions of scatter of the entropy/free-energy from the dominant KBM $(k_x\rho_i, k_y\rho_i) = (\pm 0.31, 0.12)$ to the high-wavenumber region in the Fourier space $\mathbf{k}_\perp = (k_x, k_y)$ (Figs. 27 and 28): one is the direction along the red arrows with "interaction with inclined mode" and the other is the direction along the blue arrows with "interaction with ZF." The amount of scatter $T(\mathbf{k}_\perp; \mathbf{k}'_\perp, \mathbf{k}''_\perp)$ is shown in Fig. 27 and is indicated by the thickness of the arrows in Fig. 28. The scatter by the inclined KBM shear is larger than that by the zonal flow shear. Hence, the mutual interaction between the dominant KBMs (inclined modes) cause the subsequent entropy transfer from the KBMs to linearly stable high-wavenumber Fourier modes.

The spectra of the electrostatic potential $\langle |\phi_{\mathbf{k}_\perp}|^2 \rangle$ for the KBM turbulence and the ITG turbulence are plotted as a function of poloidal wavenumber k_y in Fig. 29. The spectrum of the KBM turbulence has a sharp peak at the dominant mode $k_y\rho_i = 0.12$, and the zonal component $k_y = 0$ and other modes are much smaller than the dominant mode. On the other hand, the spectrum of the ITG turbulence widely spreads over k_y, and the amplitude of the zonal component is comparable with the dominant ITG modes. The energy flux due to ITG is about 5 $n_0 T_i v_{Ti} \rho_i^2 / L_n^2$, while the flux due to KBM is about 3 $n_0 T_i v_{Ti} \rho_i^2 / L_n^2$. Thus, their turbulent transports are comparable in the gyro-Bohm unit, even though the amplitude of the KBM turbulence is larger than that of the ITG turbulence (Fig. 29). This implies that the KBM turbulence is not efficient in the transport compared with the ITG turbulence [39, 42].

The finite beta turbulence is saturated by the nonlinear interactions of oppositely inclined convection cells through mutual shearing, even when the zonal flow is weak. The mechanism may also play a role in the saturation of turbulence in finite-beta tokamaks in the presence of three-dimensionality such as toroidal ripples and resonant magnetic perturbation (RMP).

9. Magnetic islands and magnetic reconnection

Electromagnetic perturbations are able to violate magnetic surfaces and cause magnetic islands through magnetic reconnection [64]. Here we briefly review gyrokinetic simulation studies on interactions between the ITG turbulence and magnetic islands and on basic physics of magnetic reconnection. Most gyrokinetic studies on the interaction of turbulence with magnetic islands consist of carrying out electrostatic simulations in the presence of a fixed magnetic island [65, 66, 67, 68], and it is reported that the production of long wavelength mode by ITG turbulence can give rise to an oscillating vortex flow inside the island separatrix [66], and the oscillation is related to the geodesic acoustic mode [67]. The momentum transport associated with a magnetic island interacting with external magnetic perturbation is also studied [68]. There are some gyrokinetic simulations of magnetic reconnection for understanding the magnetic island formation. The dependence of instabilities associated with magnetic reconnection on collisions is reported in Ref. [69]. The acceleration of magnetic reconnection, which was found by fluid simulations, is confirmed [70]. It is also found that collisionless magnetic reconnection is reversible [71]. The electromagnetic gyrokinetic simulations of microturbulence interacting with self-consistently produced magnetic islands in global geometry are retained for future work.

10. Summary

Electromagnetic gyrokinetic simulation enables us to study turbulent transport in finite beta torus plasmas. When the plasma beta is small, the ITG and TEM/ETG modes are unstable, and the ITG turbulence is regulated by zonal flows. Magnetic perturbation with tearing parity can be produced from the ITG mode, which has ballooning parity, through nonlinear interactions, and can influence turbulent transport by violating magnetic surface.

When the beta is increased with keeping the magnetic field, density, and temperature profiles, the growth rate of ITG mode decreases, while the zonal flow amplitude is not so influenced, and thus the turbulent transport is reduced. When plasma beta exceeds a critical value, the zonal flows are weak, and then the turbulent transport becomes very large correspondingly. This unphysical large transport is observed not only for CBC but also for other DIII-D cases [22]. The magnetic perturbation plays a central role in reducing the growth rate of ITG, and probably in weak zonal flow production. The KBM, which is an electromagnetic instability, is destabilized at high beta, and a saturation of the KBM turbulence is obtained even when the zonal flows are weak, when the electron temperature gradient is set to be small and beta value is just above the linear instability threshold. The mode structure along the magnetic field line plays a role in the saturation of turbulence, and thus the saturation level is influenced by the length of simulation domain along the magnetic field line. The spectrum of the KBM turbulence is much narrower than that of ITG turbulence and the efficiency in transport is small compared with the ITG turbulence at low beta. The condition for getting a physically relevant saturation level of ITG/TEM turbulence at finite beta and KBM turbulence at high beta has not been fully understood yet.

The analysis of simulation results based on some basic properties of the electromagnetic gyrokinetic equation is emphasized. One is the conservation of the

quadratic quantity called entropy variable, and another is the parity invariance of the linearized gyrokinetic equation. Saturation process of turbulence can be clarified by investigating the nonlinear entropy transfer in the Fourier space and by examining the nonlinear exchange of parities of perturbation against the coordinate along the magnetic field line.

Acknowledgements

One of the authors A. I. thanks Prof. S. Benkadda and Prof. K. Itoh for their support, and also thanks Prof. Y. Kishimoto for fruitful discussion. This work is supported by the Japanese Ministry of Education, Culture, Sports, Science and Technology (Grant No. 23561003) and by NIFS Collaborative Research Program (NIFS14KNTT027 and NIFS14KNST067). The numerical simulations were carried out on the Plasma Simulator at National Institute for Fusion Science and the Helios Super Computer System at Computational Simulation Center of International Fusion Energy Research Center.

References

[1] W. Horton, *Turbulent transport in magnetized plasmas*, World Scientific, (2012).
[2] J. Wesson, *Tokamaks*, Oxford University Press, (2004).
[3] J. Freidberg, *Plasma Physics and Fusion Energy*, Cambridge, (2007).
[4] P. Helander and D. J. Sigmar, *Collisional Transport in Magnetized Plasmas*, Cambridge, (2002).
[5] A. B. Rechester and M. N. Rosenbluth, Phys. Rev. Lett. **40**, 38 (1978).
[6] A. M. Dimits, et. al., Phys. Plasmas **7**, 969 (2000).
[7] T. M. Antonsen and B. Lane, Phys. Fluids **23**, 1205 (1980).
[8] E. A. Frieman and L Chen, Phys. Fluids **25**, 502 (1982).
[9] T. S. Hahm, W. W. Lee, and A. Brizard, Phys. Fluids **31**, 1940 (1988).
[10] A. J. Brizard and T. S. Hahm, Rev. Mod. Phys. **79**, 421 (2007).
[11] R. D. Hazeltine and J. D. Meiss, *Plasma Confinement*, Dover, (2003).
[12] M. Kotschenreuther, G. Rewoldt, and W. M. Tang, Computer Physics Communications **88**, 128 (1995).
[13] F. Jenko, Computer physics communications **125**, 196 (2000).
[14] F. Jenko, W. Dorland, M. Kotschenreuther, and B. N. Rogers, Phys. Plasmas **7**, 1904 (2000).
[15] F. Jenko and W. Dorland, Plasma Physics and Controlled Fusion **43**, A141 (2001).
[16] J. Candy and R. E. Waltz, Journal of Computational Physics **186**, 545 (2003).
[17] J. Candy and R. E. Waltz, Phys. Rev. Lett. **91**, 045001 (2003).
[18] J. Candy, Phys. Plasmas **12**, 072307 (2005).
[19] M. J. Pueschel, M. Kammerer, and F. Jenko, Phys. Plasmas **15**, 102310 (2008).
[20] A. G. Peeters, Y. Camenen, F. J. Casson, W. A. Hornsby, A. P. Snodina, D. Strintzi, and G. Szepesia, Computer Physics Communications **180**, 2650 (2009).
[21] M. J. Pueschel and F. Jenko, Phys. Plasmas **17**, 062307 (2010).
[22] R. E. Waltz, Phys. Plasmas **17** 072501 (2010).

[23] D. R. Hatch, M. J. Pueschel, F. Jenko, W. M. Nevins, P. W. Terry, and H. Doerk, Phys. Rev. Lett. **108**, 235002 (2012).
[24] M. J. Pueschel, P. W. Terry, F. Jenko, D. R. Hatch, W. M. Nevins, T. Gorler, and D. Told, Phys. Rev. Lett. **110**, 155005 (2013).
[25] M. J. Pueschel, T. Gorler, F. Jenko, D. R. Hatch, and A. J. Cianciara ,Phys. Plasmas **20**, 102308 (2013).
[26] M. A. Beer, S. C. Cowley and G. W. Hammett, Phys. Plasmas **2**, 2687 (1995).
[27] A. A. Schekochihin, S. C. Cowley, W. Dorland, G. W. Hammett, G. G. Howes, E. Quataert, and T. Tatsuno, The Astrophysical Journal Supplement Series **182**, 310 (2009)
[28] J. Y. Kim, W. Horton and J. Q. Dong, Phys. Fluids **B 5**, 4030 (1993).
[29] P. W. Terry, M. J. Pueschel, D. Carmody and W. M. Nevins, Phys. Plasmas **20**, 112502 (2013).
[30] P. W. Terry, D. Carmody, H. Doerk, W. Guttenfelder, D. R. Hatch, C. C. Hegna, A. Ishizawa, F. Jenko, W. M. Nevins, I. Predebon, M. J. Pueschel, J. S. Sar and G. G. Whelan, IAEA-FEC, OV/5-1 (2014).
[31] M. J. Pueschel, P. W. Terry and D. R. Hatch, Phys. Plasmas **21**, 055901 (2014).
[32] W. M. Tang, J. W. Connor, R. J. Hastie, Nucl. Fusion **20**, 1439 (1980).
[33] A. Hirose, Phys. Rev. Lett. **72**, 3993 (1994).
[34] T.-H. Watanabe and H. Sugama, Nuclear Fusion **46**, 24 (2006).
[35] A. Ishizawa, S. Maeyama, T.-H. Watanabe, H. Sugama, and N. Nakajima, Nuclear Fusion **53**, 053007 (2013).
[36] S. Maeyama, A. Ishizawa, T.-H. Watanabe, N. Nakajima, S. Tsuji-Iio, and H. Tsutsui, Computer Physics Communications **184**, 2462 (2013).
[37] H. Sugama, T.-H. Watanabe, and M. Nunami, Phys. Plasmas **16** 112503 (2009).
[38] A. Ishizawa, T.-H. Watanabe and N. Nakajima, Plasma Fusion Research **6**, 2403087 (2011).
[39] S. Maeyama, A. Ishizawa, T.-H. Watanabe, M. Nakata, N. Miyato, M. Yagi, and Y. Idomura, Phys. Plasmas **21**, 052301 (2014).
[40] T.-H. Watanabe and H. Sugama, Phys. Plasmas **11**, 1476 (2004).
[41] H. Sugama, M. Okamoto, W. Horton, and M. Wakatani, Phys. Plasmas **3**, 2379 (1996).
[42] A. Ishizawa, T.-H. Watanabe, H. Sugama, S. Maeyama, and N. Nakajima, Phys. Plasmas **21**, 055905 (2014).
[43] M. Nakata, T.-H. Watanabe, and H. Sugama, Phys. Plasmas **19**, 022303 (2012).
[44] A. G. Peeters, C. Angioni, and the ASDEX Upgrade Team, Phys. Plasmas **12**, 072515 (2005).
[45] H. Sugama, T.-H. Watanabe, M. Nunami, and S. Nishimura, Plasma Phys. Control. Fusion **53**, 024004 (2011).
[46] B. D. Fried, and S. D. Conte, The Plasma Dispersion Function (Academic Press, New York NY) (1961).
[47] L. Chen, Plasma Phys. Control. Fusion **50**, 124001 (2008).
[48] P. C. Clemmow and J. P. Dougherty, Electrodynamics of Particles and Plasmas (Redwood City: Addison-Wesley) (1969).
[49] O. Kaneko H. Yamada, S. Inagaki, and LHD Experiment Group, Nuclear Fusion **53**, 104015 (2013).

[50] T.-H. Watanabe, H. Sugama, S.F. Margalet, Phys. Rev. Lett. **100**, 195002 (2008).
[51] S. Ohdachi, K. Tanaka, K.Y. Watanabe, and LHD Experiment Group, Cont. Plasma Phys. **50**, 552 (2010).
[52] S. Ferrando-Margalet, H. Sugama, and T.-H. Watanabe, Phys. Plasmas **14**, 122505 (2007).
[53] D. J. Applegate, C. M. Roach, J. W. Connor, S. C. Cowley, W. Dorland, R. J. Hastie and N. Joiner, Plasma Phys. Control. Fusion **49**, 1113 (2007).
[54] D. Told, F. Jenko, P. Xanthopoulous, L. D. Horton, E. Wolfrum, and ASDEX Upgrade Team, Phys. Plasmas **15**, 102306 (2008).
[55] H. Doerk, F. Jenko, M. J. Pueschel and D. R. Hatch, Phys. Rev. Lett. **106**, 155003 (2011).
[56] W. Guttenfelder, J. Candy, S. M. Kaye, W. M. Nevins, E. Wang, R. E. Bell, G. W. Hammett, B. P. LeBlanc, D. R. Mikkelsen, and H. Yuh, Phys. Rev. Lett. **106**, 155004 (2011).
[57] W. Guttenfelder, J. Candy, S. M. Kaye, W. M. Nevins, R. E. Bell, G. W. Hammett,B. P. LeBlanc and H. Yuh, Phys. Plasmas **19**, 022506 (2012).
[58] H. Sugama and T.-H. Watanabe, Phys. Plasmas **11**, 3068 (2004).
[59] P. A. Davidson, *Turbulence*, (Oxford University Press, 2004).
[60] P. H. Diamond, S.-I. Itoh, and K. Itoh, *Modern Plasma Physics*, (Cambridge University Press, 2010).
[61] T. Gorler, et.al., Phys. Rev. Lett. **100**, 185002 (2008).
[62] S. Maeyama, Y. Idomura, M. Nakata, M. Yagi, and N. Miyato, IAEA-FEC TH/1-1, (2014).
[63] S. Maeyama, A. Ishizawa, T.-H. Watanabe, M. Nakata, N. Miyato and Y. Idomura, Plasma Fusion Res. **9**, 1203020 (2014).
[64] D. Biskamp, *Magnetic Reconnection in Plasmas*, (Cambridge University Press, Cambridge, 2000).
[65] E. Poli, A. Bottino and A.G. Peeters, Nucl. Fusion **49**, 075010 (2009).
[66] W. A. Hornsby, M. Siccinio, A. G. Peeters, E. Poli, A. P. Snodin, F. J. Casson, Y. Camenen, and G. Szepesi, Plasma Phys. Control. Fusion **53**, 054008 (2011).
[67] W. A. Hornsby, A. G. Peeters, M. Siccinio, and E. Poli, Phys. Plasmas **19**, 032308 (2012).
[68] R. E. Waltz and F. L. Waelbroeck, Phys. Plasmas **19**, 032508 (2012).
[69] R. Numata, W. Dorland, G. G. Howes, N. F. Loureiro, B. N. Rogers and T. Tatsuno, Phys. Plasmas **18**, 112106 (2011).
[70] M. J. Pueschel, F. Jenko, D. Told, and J. Buchner, Phys. Plasmas **18**, 112102 (2011).
[71] A. Ishizawa and T.-H. Watanabe, Physics of Plasmas, **20**, 102116 (2013).

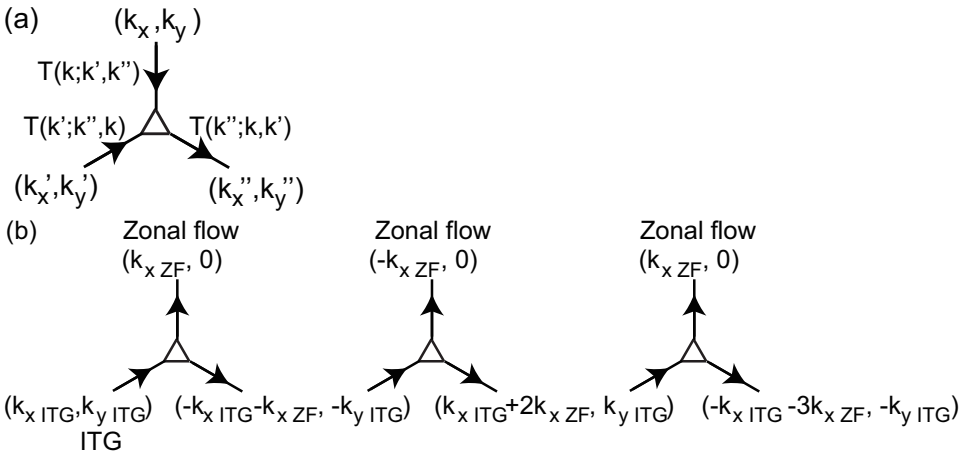

Figure 1. The diagram of nonlinear entropy transfer in the Fourier space: (a) an element is a triangle with the vertexes connected to three lines representing three energy transfer functions of the mode at the other end of the line, $T(\mathbf{k}_\perp;\mathbf{k}'_\perp,\mathbf{k}''_\perp)$, $T(\mathbf{k}'_\perp;\mathbf{k}''_\perp,\mathbf{k}_\perp)$ and $T(\mathbf{k}''_\perp;\mathbf{k}_\perp,\mathbf{k}'_\perp)$, where $T(\mathbf{k}_\perp;\mathbf{k}'_\perp,\mathbf{k}''_\perp)+T(\mathbf{k}'_\perp;\mathbf{k}''_\perp,\mathbf{k}_\perp)+T(\mathbf{k}''_\perp;\mathbf{k}_\perp,\mathbf{k}'_\perp)=0$ and the arrows represent the signs of them, which are $T(\mathbf{k}_\perp;\mathbf{k}'_\perp,\mathbf{k}''_\perp)<0$, $T(\mathbf{k}'_\perp;\mathbf{k}''_\perp,\mathbf{k}_\perp)<0$ and $T(\mathbf{k}''_\perp;\mathbf{k}_\perp,\mathbf{k}'_\perp)>0$ in the figure as an example, and (b) an example showing the transfer for the ITG turbulence regulated by zonal flows which scatter the entropy of the ITG mode to a high wavenumber region.

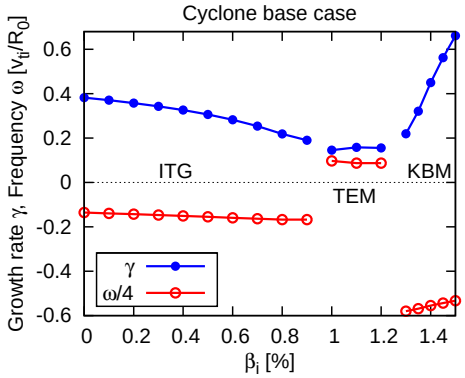

Figure 2. Growth rate and real frequency of microturbulence in CBC for $k_y\rho_{Ti}=0.2$ as a function of ion beta β_i.

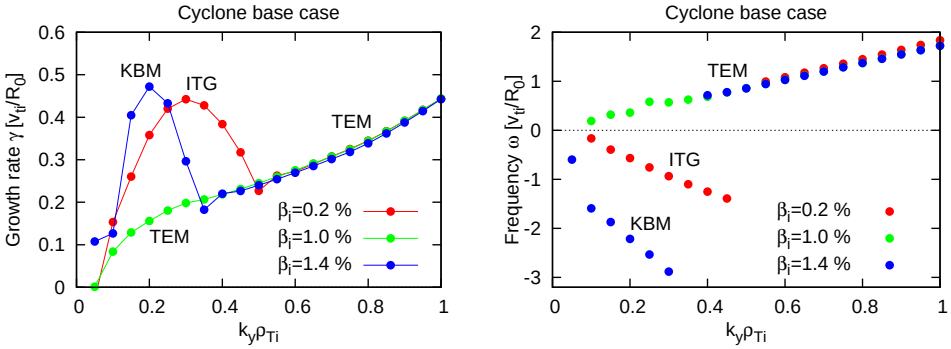

Figure 3. Growth rate and real frequency of microturbulence in CBC as a function of poloidal wavenumber k_y for several ion beta.

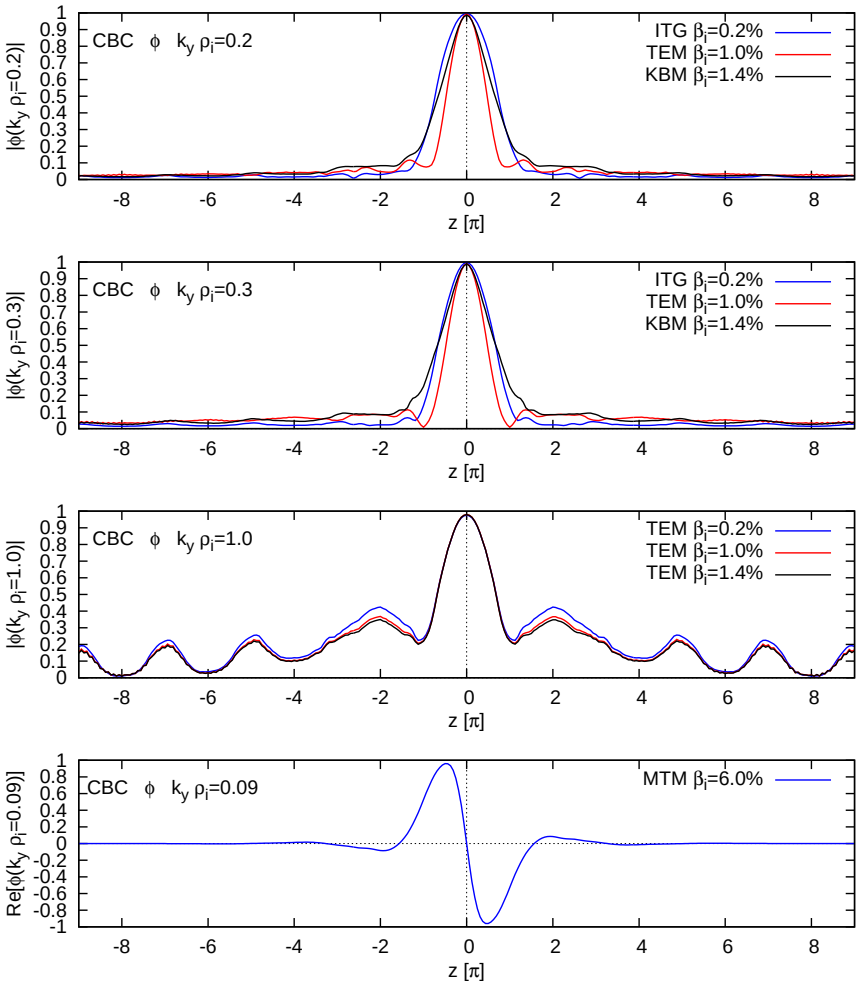

Figure 4. Profile of electrostatic potential ϕ along the magnetic field line z for $k_y\rho_{Ti} = 0.3$, which is the most unstable ITG mode in Fig. 3; for $k_y\rho_{Ti} = 0.2$, which is the most unstable KBM in Fig. 3; for $k_y\rho_{Ti} = 1.0$, which is the most unstable TEM in Fig. 3; and for $k_y\rho_{Ti} = 0.09$ of TEM. The ITG mode, TEM, and KBM are classified into the ballooning parity mode, while the MTM is classified into the tearing parity mode.

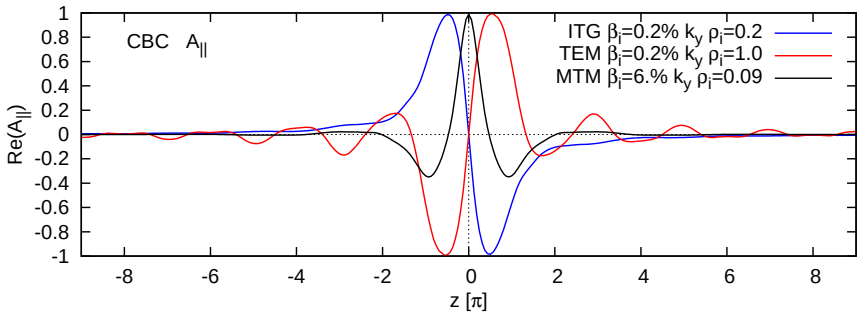

Figure 5. Profile of the parallel component of the vector potential $A_{\parallel}$ along the magnetic field line z for ITG with $k_y\rho_{Ti} = 0.2$, TEM with $k_y\rho_{Ti} = 1.0$, and MTM with $k_y\rho_{Ti} = 0.09$. The ITG mode and TEM are an odd function of z and are classified into the ballooning parity mode. On the other hand, the MTM is an even function of z and is classified into the tearing parity mode. The vector potential has the opposite parity as the electrostatic potential in Fig. 4.

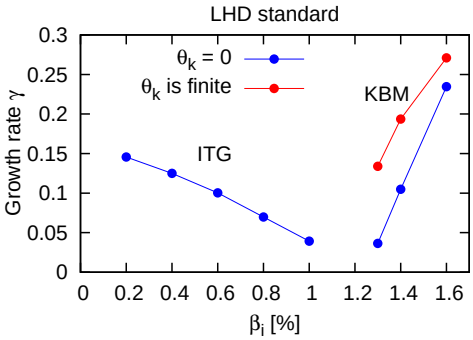

Figure 6. Growth rate of micro-instability in a helical plasma as a function of ion beta.

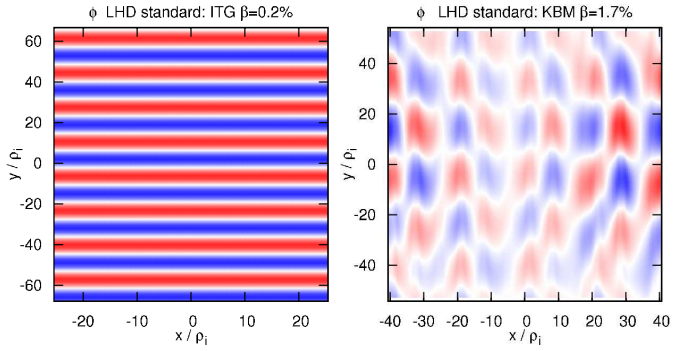

Figure 7. Profile of electrostatic potential ϕ of the ITG mode at $\beta_i = 0.2\%$ and of the most unstable KBM at $\beta_i = 1.7\%$ on (x, y) plane for LHD with $\eta_e = 0$.

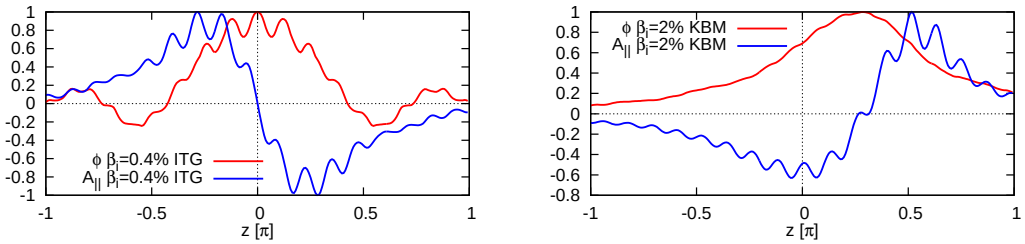

Figure 8. Profile of electrostatic potential ϕ and parallel component of vector potential $A_\parallel$ of the most unstable ITG at $\beta_i = 0.2\%$ and of the most unstable KBM at $\beta_i = 1.7\%$ along the magnetic field line z for LHD with $\eta_e = 0$.

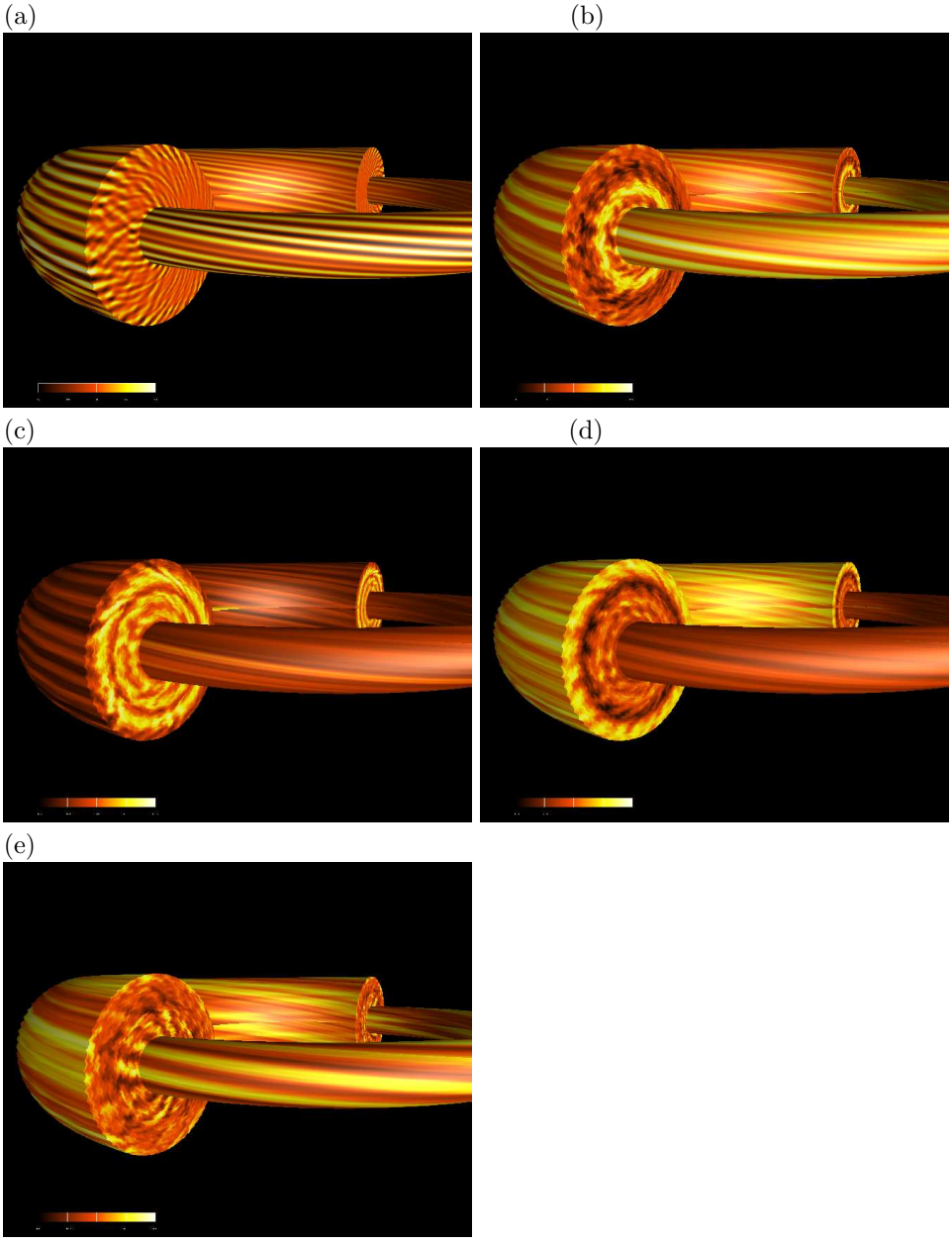

Figure 9. Color map of the electrostatic potential profile in the configuration space, at (a) growing phase for $\beta_i = 0.2\%$, (b) statistically steady state for $\beta_i = 0.2\%$, (c) statistically steady state for $\beta_i = 0.4\%$, (d) statistically steady state for $\beta_i = 0.6\%$, and (e) nonlinear growing phase for $\beta_i = 0.8\%$.

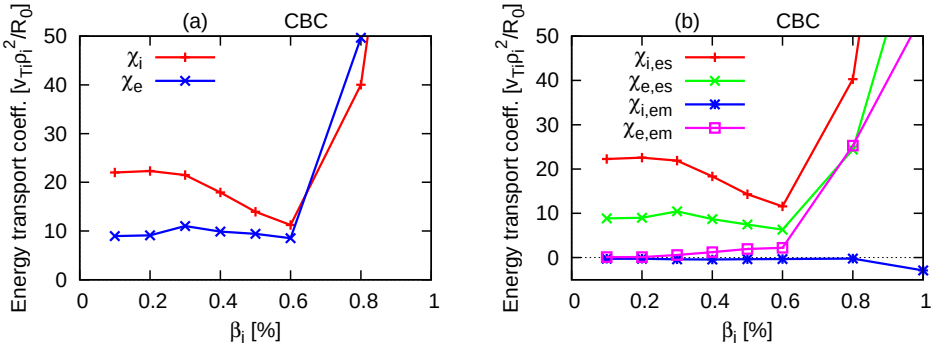

Figure 10. The ion beta β_i dependence of (a) time averaged energy diffusion coefficient and (b) the coefficient due to the electrostatic perturbation $\chi_{s,es}$ and magnetic perturbation $\chi_{s,em}$.

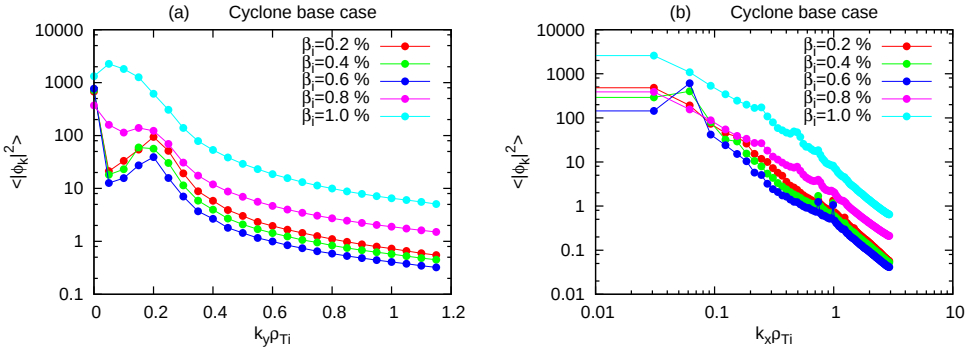

Figure 11. Spectra of the electrostatic potential for several β_i as a function of (a) the poloidal wavenumber k_y and (b) the radial wavenumber k_x.

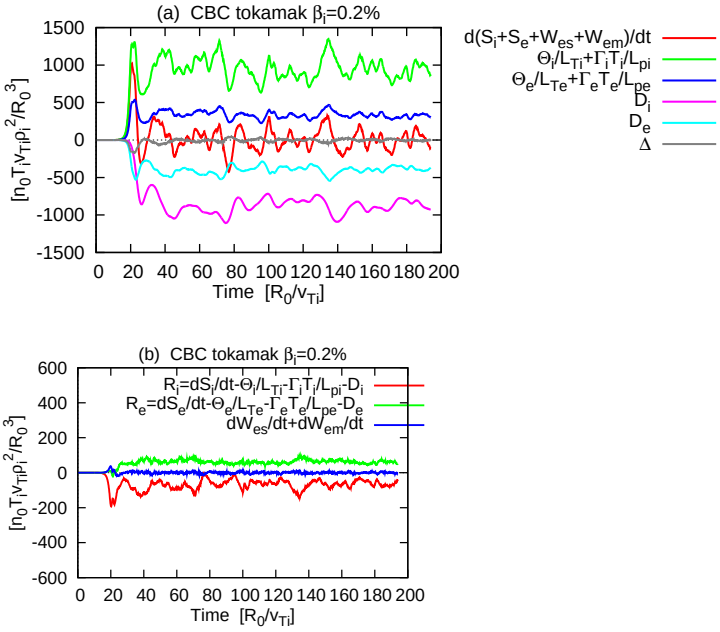

Figure 12. Each term in the entropy balance equation Eq. (3.1) for ITG turbulence with $\beta_i = 0.2\%$ in CBC. The entropy balance error Δ is much smaller than the entropy production term (free energy term) of ions $\Theta_i/L_{Ti} + \Gamma_i T_i/L_{pi}$. Each term of Eq. (3.12) showing the entropy transfer from ions to electrons.

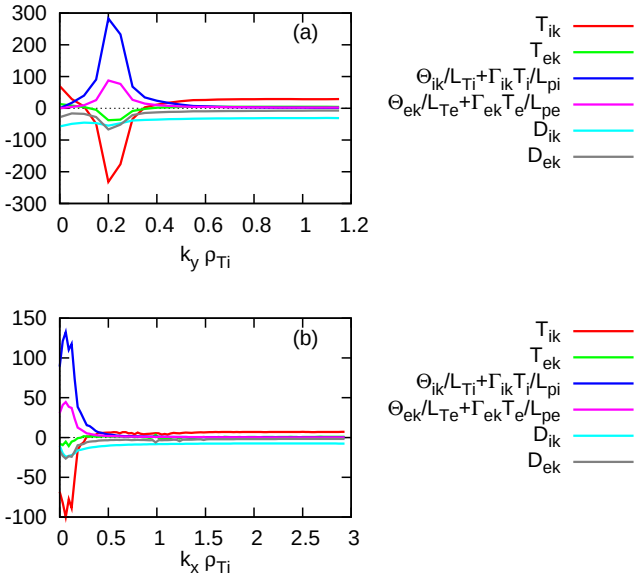

Figure 13. Each term in the entropy balance equation for a wavenumber $\mathbf{k}_\perp$ Eq. (3.14) for the ITG turbulence in CBC with $\beta_i = 0.2\%$ (a) the entropy transfer function $\mathcal{T}_{s,k_y} = \sum_{k_x} \mathcal{T}_{s\mathbf{k}_\perp}$, the entropy production $\Theta_{s,k_y}/L_{Ts} + \Gamma_{s,k_y} T_s/L_{ps} = \sum_{k_x} \Theta_{s\mathbf{k}_\perp}/L_{Ts} + \Gamma_{s\mathbf{k}_\perp} T_s/L_{ps}$, and the collisional dissipation $D_{s,k_y} = \sum_{k_x} D_{s\mathbf{k}_\perp}$ as a function of poloidal wavenumber k_y (b) $\mathcal{T}_{s,k_x} = \sum_{k_y} \mathcal{T}_{s\mathbf{k}_\perp}$, $\Theta_{s,k_x}/L_{Ts} + \Gamma_{s,k_x} T_s/L_{ps}$, and D_{s,k_x} as a function of radial wavenumber k_x. The anisotropy of the transport in the Fourier space is significant.

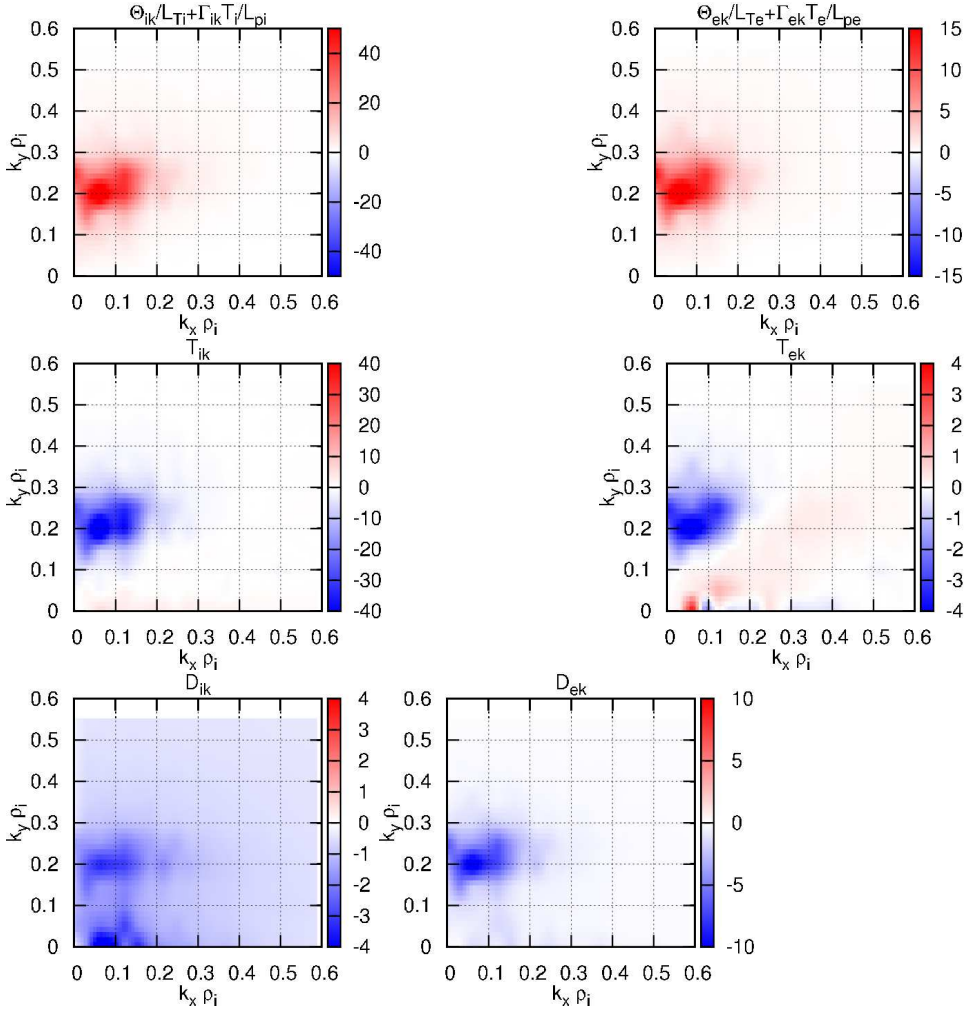

Figure 14. Each term in the entropy balance equation for a wavenumber $\mathbf{k}_\perp$ in Eq. (3.14), the entropy production $\Theta_{s\mathbf{k}_\perp}/L_{Ts} + \Gamma_{s\mathbf{k}_\perp} T_s/L_{ps}$, the entropy transfer function $\mathcal{T}_{s\mathbf{k}_\perp}$, and the collisional dissipation $D_{s\mathbf{k}_\perp}$, for the ITG turbulence in CBC with $\beta_i = 0.2\%$ on the $\mathbf{k}_\perp = (k_x, k_y)$ plane. The anisotropy of the entropy transport in the $\mathbf{k}_\perp = (k_x, k_y)$ space is significant.

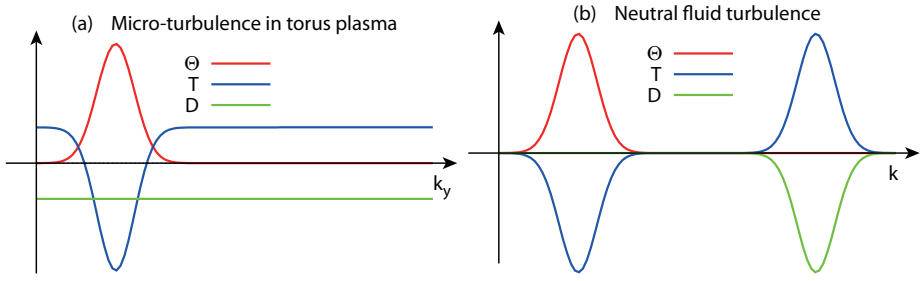

Figure 15. Schematic graphs of the drive of free energy Θ, the transfer function T, and the dissipation D for (a) the entropy transfer of the micro-turbulence in torus plasmas and (b) the energy transfer of neutral fluid turbulence.

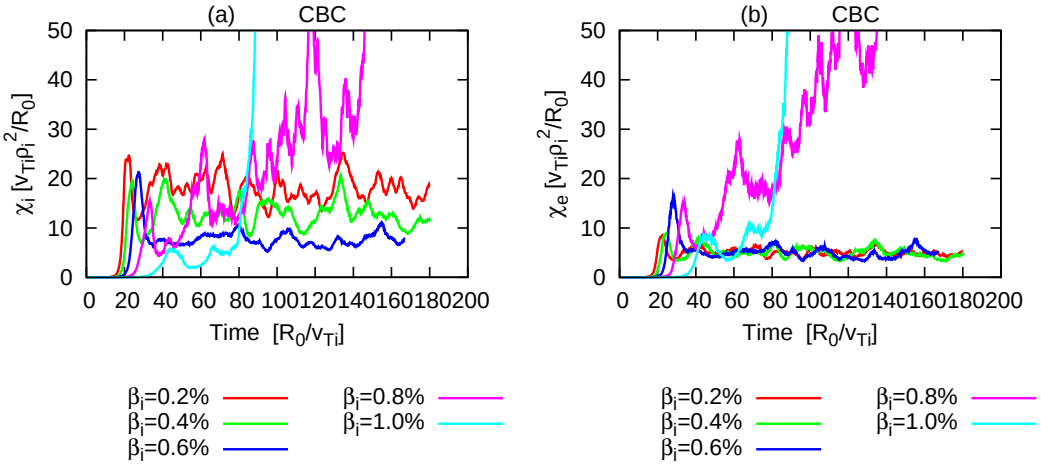

Figure 16. Time evolution of ion and electron energy diffusion coefficient χ_i and χ_e for several β_i.

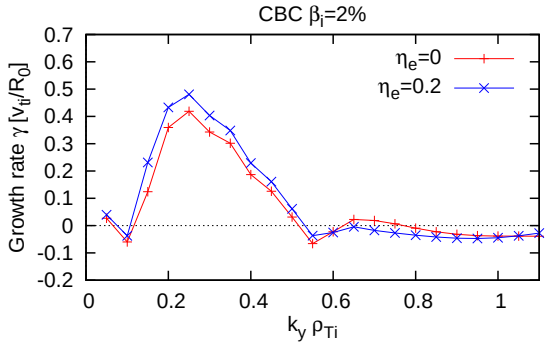

Figure 17. Growth rate of KBM in CBC for $\eta_e = 0$ and 0.2 as a function of the poloidal wavenumber k_y.

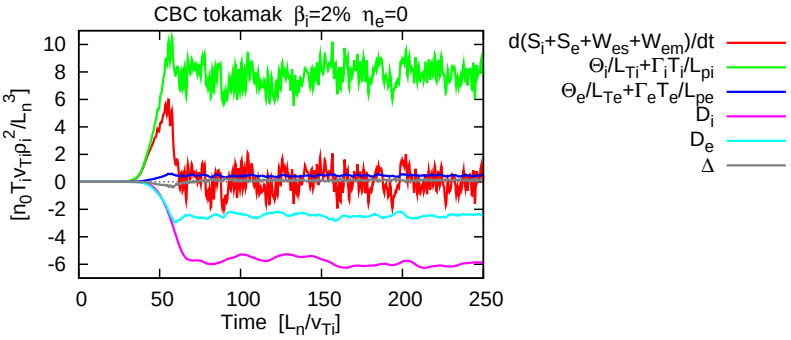

Figure 18. Each term in the entropy balance equation for KBM turbulence with $\beta_i = 2\%$ and $\eta_e = 0$ in CBC.

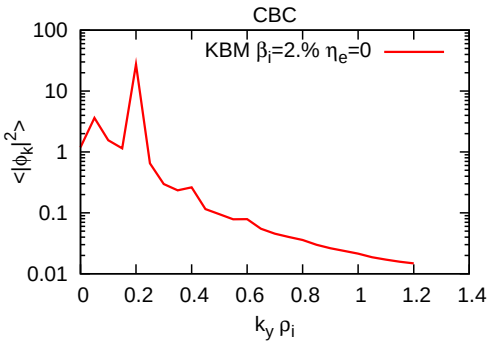

Figure 19. Spectrum of the electrostatic potential of KBM turbulence for CBC with $\beta_i = 2.\%$ and $\eta_e = 0$.

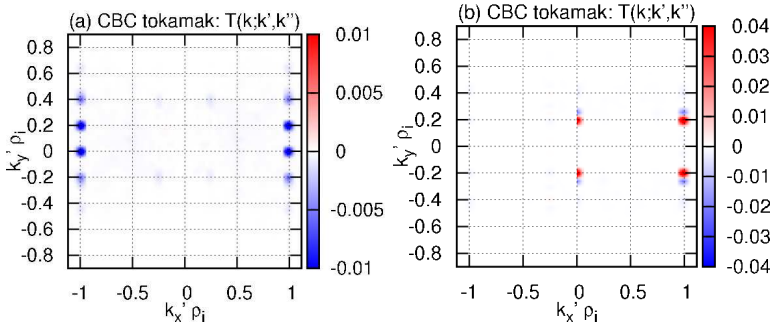

Figure 20. Entropy transfer function $\mathcal{T}(\mathbf{k}_\perp; \mathbf{k}'_\perp, \mathbf{k}''_\perp)$ averaged from $t = 50$ to 60 for the KBM turbulence with $\beta = 2\%$ in CBC plasma on $\mathbf{k}'_\perp$ plane for (a) $\mathbf{k}_\perp = (\rho_i k_x, \rho_i k_y) = (0, 0.2)$ and (b) $\mathbf{k}_\perp = (\rho_i k_x, \rho_i k_y) = (1., 0)$. It is noted that $\mathbf{k}'_\perp$ satisfies $\mathbf{k}'_\perp = \mathbf{k}_\perp - \mathbf{k}''_\perp$.

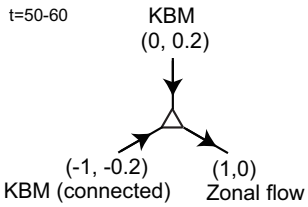

Figure 21. The diagram of the nonlinear entropy transfer in the Fourier space for the KBM turbulence in CBC with $\beta_i = 2\%$, $\eta_i = 3.1$, and $\eta_e = 0$: the arrow from $\mathbf{k}_\perp = (k_x, k_y) = (0, 0.2)$ shows the transfer of the entropy/free-energy from the dominant KBM to zonal flow through the connected mode $\mathbf{k}_\perp = (k_x, k_y) = (1, 0.2)$.

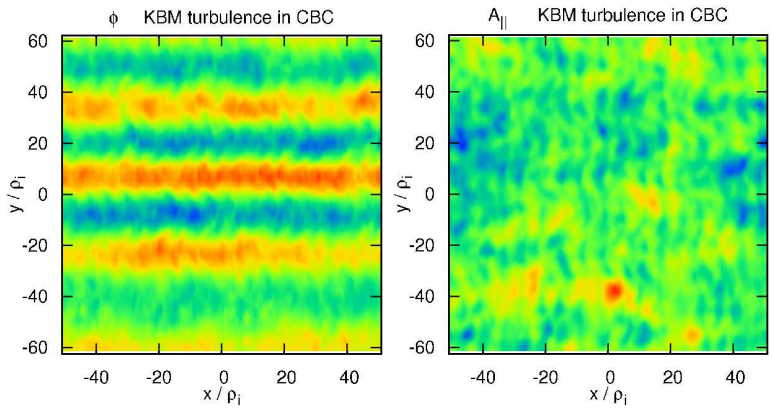

Figure 22. The fluctuation of KBM turbulence on $z = 0$ plane in the steady state: (a) electrostatic potential and (b) parallel component of the vector potential profiles, where x and y are in the radial and poloidal directions, respectively.

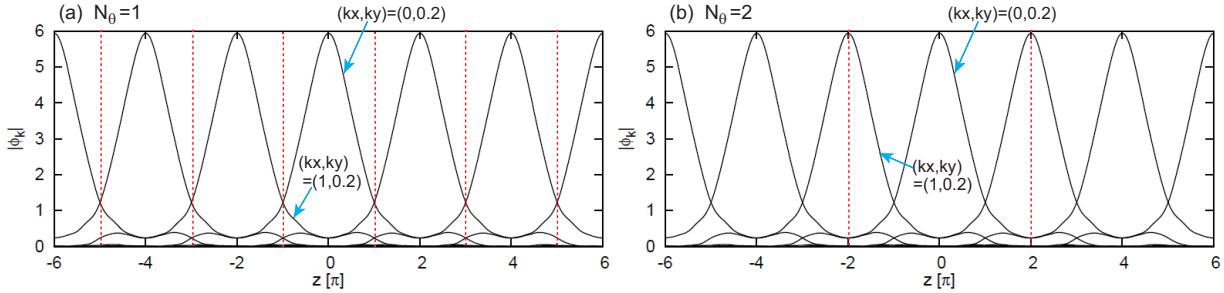

Figure 23. Electrostatic potential profile of (a) the KBM with $\mathbf{k}_\perp = (k_x, k_y) = (0, 0.2)$ and the connected mode $(k_x, k_y) = (1, 0.2)$ in the simulation domain $-\pi \leqslant z \leqslant \pi$ $(N_\theta = 1)$ and (b) the KBM with $\mathbf{k}_\perp = (k_x, k_y) = (0, 0.2)$ and the other KBM with $(k_x, k_y) = (1, 0.2)$ in the simulation domain $-2\pi \leqslant z \leqslant 2\pi$ $(N_\theta = 2)$. The simulation boxes divided the dotted red lines are identical.

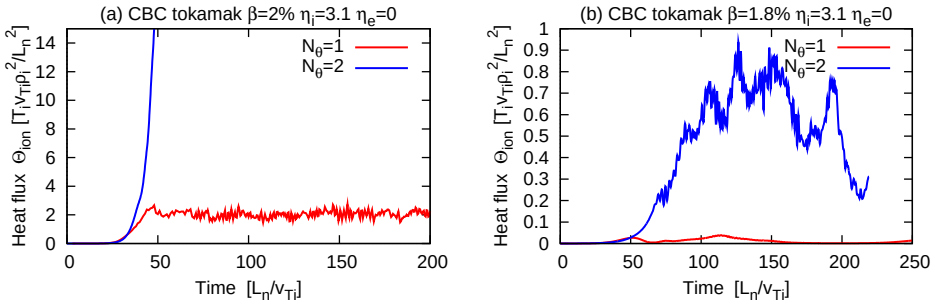

Figure 24. Time evolution of heat flux caused by KBM turbulence in CBC plasma with $\eta_e = 0$ and (a) $\beta = 2\%$ and (b) $\beta = 1.8\%$ with the flux tube length $-N_\theta\pi \leqslant z \leqslant N_\theta\pi$ for $N_\theta = 1$ and $N_\theta = 2$.

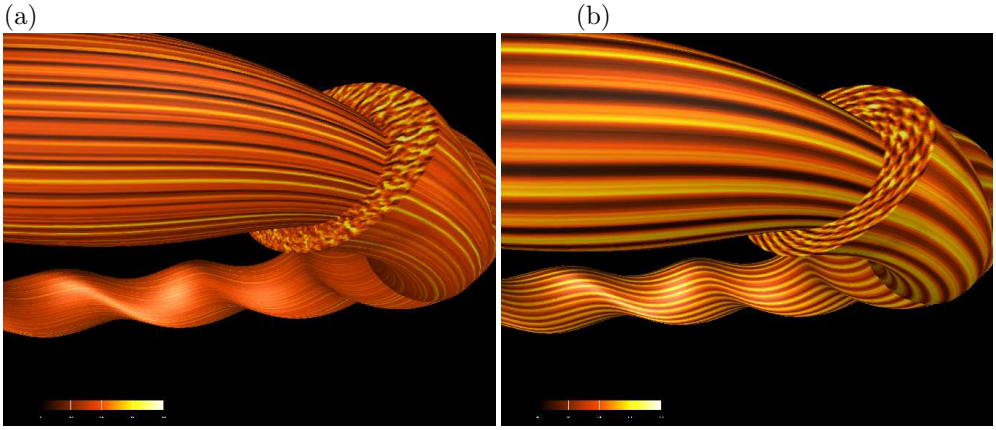

Figure 25. Electrostatic potential profile of (a) the ITG turbulence with very small beta and (b) the KBM turbulence with finite beta in a helical plasma. The KBM is saturated by the interactions with oppositely inclined modes, while the ITG is regulated by zonal flows.

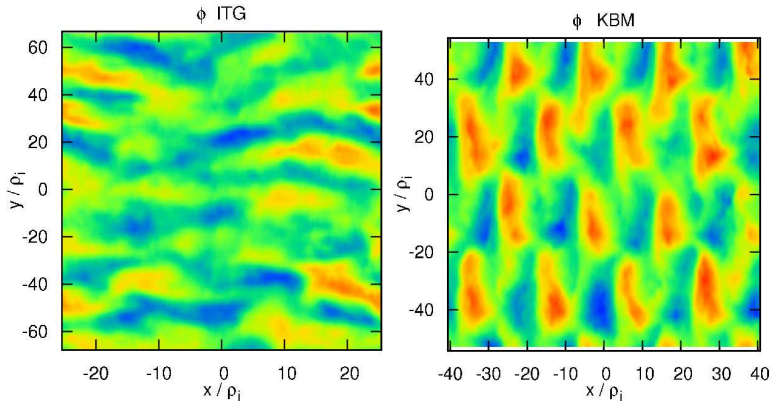

Figure 26. Electrostatic potential profile of the ITG turbulence with very small beta and the KBM turbulence with finite beta in a helical plasma on the $z = 0$ plane, where x and y are in the radial and poloidal directions, respectively.

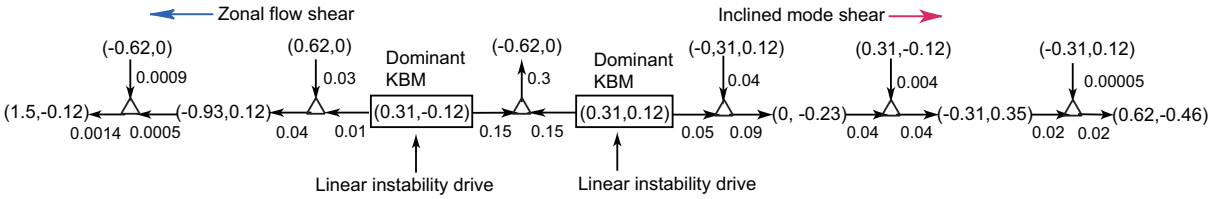

Figure 27. The diagram of the nonlinear entropy transfer for the KBM turbulence in LHD with $\beta_i = 1.7\%$, $\eta_i = 3$, and $\eta_e = 0$.

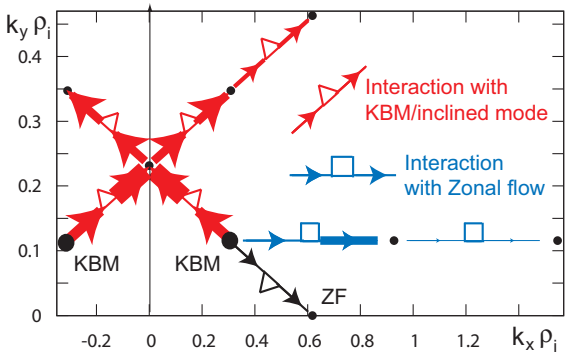

Figure 28. Entropy transfer in the wavenumber space (k_x, k_y) of the KBM turbulence in LHD. The red (blue) arrows show the scatter from the dominant KBM $(k_x\rho_i, k_y\rho_i) = (\pm 0.31, 0.12)$ to the stable high-wavenumber modes by the inclined mode (zonal flow) shear. The thickness of the arrows show the amount of transfer.

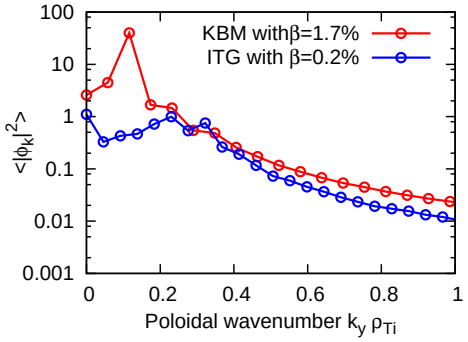

Figure 29. Spectrum of electrostatic potential $\langle|\phi_{\mathbf{k}_\perp}|^2\rangle$ for ITG and KBM turbulence. The spectrum of KBM turbulence is sharply peaked, while that of the ITG turbulence is broadened. The zonal component $(k_y = 0)$ of KBM is much smaller than the sharp peak of KBM in a helical plasma.

Appendix A

We present the dimensional form of the gyrokinetic equation in this appendix. The distribution functions of gyro-centers are divided into the Maxwellian part and a perturbed part, $F_s = F_{Ms} + \delta f_s$, where $F_{Ms} = \frac{n_0}{(2\pi T_s/m_s)^{3/2}} \exp(-\frac{m_s v_\parallel^2}{2T_s} - \frac{\mu B}{T_s})$. The gyrokinetic equation is

$$\begin{aligned}
&\frac{\partial \delta f_{s\mathbf{k}_\perp}}{\partial t} + v_\parallel \mathbf{b}_s^* \cdot \nabla \delta f_{s\mathbf{k}_\perp} - \frac{\mu}{m_s}\mathbf{b}\cdot\nabla B \frac{\partial \delta f_{s\mathbf{k}_\perp}}{\partial v_\parallel} \\
&= -i\mathbf{v}_{ds}\cdot\mathbf{k}_\perp \left(\delta f_{s\mathbf{k}_\perp} + \frac{q_s}{T_s} F_{Ms}\phi_{\mathbf{k}_\perp} J_{0s}\right) - (\tilde{\mathbf{v}}_{Es}\cdot\nabla\delta f_s)_{\mathbf{k}_\perp} \\
&\quad + i\mathbf{v}_{*s}\cdot\mathbf{k}_\perp \frac{q_s}{T_s} F_{Ms}\left(\phi_{\mathbf{k}_\perp} - \frac{v_\parallel}{c} A_{\parallel\mathbf{k}_\perp}\right) J_{0s} + v_\parallel \frac{q_s}{T_s} F_{Ms} E_{\parallel s\mathbf{k}_\perp} + C_s, \qquad \text{(A 1)}
\end{aligned}$$

where $E_{\parallel s\mathbf{k}_\perp} = -(\mathbf{b}_s^*\cdot\nabla J_{0s}\phi)_{\mathbf{k}_\perp} - \frac{1}{c}\frac{\partial}{\partial t} A_{\parallel\mathbf{k}_\perp} J_{0s}$, $q_i = e$, $q_e = -e$, and $J_{0s} = J_0(\rho_s k_\perp)$ is the zeroth order Bessel function. In the equations $(\tilde{\mathbf{v}}_{Es}\cdot\nabla\delta f_s)_{\mathbf{k}_\perp} = \frac{c}{B}[\phi J_{0s}, \delta f_s]_{\mathbf{k}_\perp}$ and $(\mathbf{b}_s^*\cdot\nabla f)_{\mathbf{k}_\perp} = \mathbf{b}\cdot\nabla f_{\mathbf{k}_\perp} - \frac{1}{B}[A_\parallel J_{0s}, f]_{\mathbf{k}_\perp}$. The drift velocities are $\mathbf{v}_{ds} = \frac{c}{q_s B}\mathbf{b}\times(\mu\nabla B + m_s v_\parallel^2 \mathbf{b}\cdot\nabla\mathbf{b})$, $\mathbf{v}_{*s} = \frac{cT_s}{q_s B}\mathbf{b}\times\nabla\ln F_{Ms}$, and $\tilde{\mathbf{v}}_{Es\mathbf{k}_\perp} = -\frac{c}{B}\phi_{\mathbf{k}_\perp} J_{0s} i\mathbf{k}_\perp \times \mathbf{b}$. The Poisson equation and the Ampère's law are

$$k_\perp^2 \phi_{\mathbf{k}_\perp} = 4\pi \sum_s q_s \left(\int \delta f_{s\mathbf{k}_\perp} J_{0s} d^3v - \frac{q_s n_0}{T_s}(1-\Gamma_{0s})\phi_{\mathbf{k}_\perp}\right), \qquad \text{(A 2)}$$

$$k_\perp^2 A_{\parallel\mathbf{k}_\perp} = \frac{4\pi}{c}\sum_s q_s \int v_\parallel \delta f_{s\mathbf{k}_\perp} J_{0s} d^3v, \qquad \text{(A 3)}$$

where $\Gamma_{0s} = e^{-\rho_s^2 k_\perp^2} I_0(\rho_s^2 k_\perp^2)$.

Appendix B

We describe physical meaning of some terms in the gyrokinetic equation Eq. (2.3) in this Appendix. When we neglect the r.h.s. of the equation and nonlinear terms, we have an equation

$$\frac{\partial}{\partial t}\delta f_{s\mathbf{k}_\perp} + v_{Ts} v_\parallel \mathbf{b}\cdot\nabla\delta f_{s\mathbf{k}_\perp} = 0. \qquad \text{(B 1)}$$

By using the flux tube coordinate introduced in Sec. 5.1, the equation is written as

$$\left(\frac{\partial}{\partial t} + v_{Ts} v_\parallel \frac{1}{qR}\frac{\partial}{\partial z}\right)\delta f_{s\mathbf{k}_\perp} = 0. \qquad \text{(B 2)}$$

The solution is a function of $z - v_{Ps}t$,

$$\delta f_{s\mathbf{k}_\perp} = g(z - v_{Ps}t), \qquad \text{(B 3)}$$

where $v_{Ps} = v_{Ts} v_\parallel/(qR)$ is the phase velocity. The solution represents the propagation of fluctuation along the magnetic field line z with the phase velocity v_{Ps}. Thus, the second term in Eq. (2.3) is responsible for the streaming of fluctuation along the magnetic field line.

Next, we consider a collisionless plasma in a uniform magnetic field $\nabla B = 0$ which implies the magnetic drift velocity vanishes $\mathbf{v}_{ds} = 0$. We further neglect the nonlinear terms, magnetic perturbation $A_\parallel = 0$, and the collision term $C = 0$. The

gyrokinetic equations Eq. (2.3) becomes

$$\frac{\partial}{\partial t}\delta f_{s\mathbf{k}_\perp} + v_{Ts}v_\parallel \mathbf{b}\cdot\nabla\delta f_{s\mathbf{k}_\perp} = v_{Ts}v_\parallel\frac{q_s}{T_s}F_{Ms}\mathbf{b}\cdot\nabla\phi_{\mathbf{k}_\perp}J_{0s} + i\mathbf{v}_{*s}\cdot\mathbf{k}_\perp\frac{q_s}{T_s}F_{Ms}\phi_{\mathbf{k}_\perp}J_{0s}. \tag{B 4}$$

A wave in this plasma $\delta f_{s\mathbf{k}_\perp} = A\exp(-i\omega t + i\mathbf{k}\cdot\mathbf{x})$ satisfies

$$(-i\omega + ik_\parallel v_\parallel v_{Ts})\delta f_{s\mathbf{k}_\perp} = (ik_\parallel v_\parallel v_{Ts} + i\omega_{*s})\frac{q_s}{T_s}F_{Ms}\phi_{\mathbf{k}_\perp}J_{0s}, \tag{B 5}$$

where $\omega_{*s} = \mathbf{v}_{*s}\cdot\mathbf{k}_\perp$. The dispersion relation is obtained by substituting this equation to the Poisson equation Eq. 2.4,

$$\lambda_{Di}^2k_\perp^2 + \sum_s\frac{q_s^2}{T_s}(1-\Gamma_{0s}) = -\sum_s\frac{q_s^2}{T_s}\int\frac{\omega_{*s}+k_\parallel v_\parallel v_{Ts}}{\omega - k_\parallel v_\parallel v_{Ts}}F_{Ms}J_{0s}^2d^3v. \tag{B 6}$$

The equation describes the Landau damping, as shown in page 36 of Ref. [1].

Appendix C

In this appendix the derivation of the entropy balance equation Eq. (3.1) is presented in detail. First we rewrite the gyrokinetic equation Eq. (2.3) in terms of the non-adiabatic part, $h_{s\mathbf{k}_\perp} = \delta f_{s\mathbf{k}_\perp} + q_s\frac{F_{Ms}}{T_s}\phi_{\mathbf{k}_\perp}J_{0s}$, to obtain Eqs. (3.18)-(3.20), where $\chi_{s\mathbf{k}_\perp} = (\phi_{\mathbf{k}_\perp} - v_\parallel A_{\parallel\mathbf{k}_\perp})J_{0s}$. Then, we multipy $\frac{h^*_{s\mathbf{k}_\perp}}{2F_{Ms}}$ to Eq. (3.18), integrate it over the velocity space, make the flux surface average, add all wavenumbers and particle species, and finally add the complex conjugate. The sum of the l.h.s. and the third term on the r.h.s. becomes

$$\begin{aligned}
&\left\langle\sum_{s,\mathbf{k}_\perp}\int d^3v\frac{T_sh^*_{s\mathbf{k}_\perp}}{2F_{Ms}}\frac{\partial}{\partial t}\left(h_{s\mathbf{k}_\perp} + q_s\frac{F_{Ms}}{T_s}\chi_{s\mathbf{k}_\perp}\right)\right\rangle + c.c.\\
&= \left\langle\sum_{s,\mathbf{k}_\perp}\int d^3v\frac{T_s\delta f^*_{s\mathbf{k}_\perp}}{2F_{Ms}}\frac{\partial\delta f_{s\mathbf{k}_\perp}}{\partial t}\right\rangle + \left\langle\sum_{\mathbf{k}_\perp}\frac{\phi^*_{\mathbf{k}_\perp}}{2}\frac{\partial}{\partial t}\left(\sum_s q_s\int d^3v\delta f_{s\mathbf{k}_\perp}J_{0s}\right)\right\rangle\\
&\quad + \left\langle\sum_{\mathbf{k}_\perp}\left(\sum_s q_sv_{Ts}\int v_\parallel\delta f_{s\mathbf{k}_\perp}J_{0s}d^3v\right)\frac{\partial}{\partial t}\frac{A_{\parallel\mathbf{k}_\perp}}{2}\right\rangle\\
&\quad + \left\langle\sum_{s,\mathbf{k}_\perp}v_{Ts}q_s^2\left(\int v_\parallel F_{Ms}J_{0s}^2d^3v\right)\phi^*_{\mathbf{k}_\perp}\frac{\partial}{\partial t}\frac{A_{\parallel\mathbf{k}_\perp}}{2}\right\rangle + c.c.\\
&= \frac{d}{dt}\left\langle\sum_{\mathbf{k}_\perp}\left[\sum_s\int d^3v\frac{T_s|\delta f_{s\mathbf{k}_\perp}|^2}{2F_{Ms}} + \left(\lambda_{Di}^2k_\perp^2 + \sum_s\frac{q_s^2}{T_s}(1-\Gamma_{0s})\right)\frac{|\phi_{\mathbf{k}_\perp}|^2}{2} + \frac{2}{\beta_i}\frac{k_\perp^2|A_{\parallel\mathbf{k}_\perp}|^2}{2}\right]\right\rangle\\
&= \frac{d}{dt}\left(\sum_s\delta S_s + W_{es} + W_{em}\right),
\end{aligned}$$

where the Poisson equation and the Ampère's law Eqs. 2.4 and 2.5 are used, $\int v_\parallel F_{Ms}J_{0s}^2d^3v = 0$, and "c.c." denotes the complex conjugate of the previous terms. The first term on the r.h.s. vanishes

$$-i\mathbf{v}_{ds}\cdot\mathbf{k}_\perp|h_{s\mathbf{k}_\perp}|^2\frac{T_s}{2F_{Ms}} + i\mathbf{v}_{ds}\cdot\mathbf{k}_\perp|h_{s\mathbf{k}_\perp}|^2\frac{T_s}{2F_{Ms}} = 0. \tag{C 1}$$

The second term on the r.h.s. vanishes

$$\begin{aligned}
&\left\langle \int d^3v \frac{T_s}{2F_{Ms}} h^*_{s\mathbf{k}_\perp} [H, h_{s\mathbf{k}_\perp}]_\parallel \right\rangle + c.c. \\
&= \left\langle \frac{T_s h^*_{s\mathbf{k}_\perp}}{2F_{Ms}} v_\parallel \nabla_\parallel h_{s\mathbf{k}_\perp} - \frac{T_s h^*_{s\mathbf{k}_\perp}}{2F_{Ms}} \mu \nabla_\parallel B \frac{\partial h_{s\mathbf{k}_\perp}}{\partial v_\parallel} \right\rangle + c.c. \\
&= \left\langle \int d^3v \nabla_\parallel \left(\frac{T_s}{2F_{Ms}} v_\parallel |h_{s\mathbf{k}_\perp}|^2 \right) \right\rangle - \left\langle \int d^3v \frac{T_s}{2F_{Ms}} v_\parallel |h_{s\mathbf{k}_\perp}|^2 \mu \nabla_\parallel B \right\rangle \\
&\quad - \left\langle \int d^3v \frac{\partial}{\partial v_\parallel} \left(\frac{T_s}{2F_{Ms}} |h_{s\mathbf{k}_\perp}|^2 \mu \nabla_\parallel B \right) \right\rangle + \left\langle \int d^3v \frac{T_s}{2F_{Ms}} v_\parallel |h_{s\mathbf{k}_\perp}|^2 \mu \nabla_\parallel B \right\rangle \\
&= 0,
\end{aligned}$$

where $\nabla_\parallel F_{Ms} = -F_{Ms} \mu \nabla_\parallel B$ and $\frac{\partial}{\partial v_\parallel} F_{Ms} = -v_\parallel F_{Ms}$ are used. The fourth term on the r.h.s. becomes

$$\begin{aligned}
&\left\langle \int d^3v i \mathbf{v}_{*s} \cdot \mathbf{k}_\perp h^*_{s\mathbf{k}_\perp} \frac{q_s}{2} \chi_{s\mathbf{k}_\perp} \right\rangle + c.c. \\
&= \left\langle \int d^3v i \mathbf{v}_{*s} \cdot \mathbf{k}_\perp \delta f^*_{s\mathbf{k}_\perp} \frac{q_s}{2} (\phi_{\mathbf{k}_\perp} - v_{Ts} v_\parallel A_{\parallel \mathbf{k}_\perp}) J_{0s} + \frac{q_s^2}{2} |\phi_{\mathbf{k}_\perp}|^2 \int d^3v i \mathbf{v}_{*s} \cdot \mathbf{k}_\perp \frac{F_{Ms}}{T_s} J_{0s}^2 \right. \\
&\quad \left. - \frac{q_s^2}{2} \phi^*_{\mathbf{k}_\perp} A_{\parallel \mathbf{k}_\perp} v_{Ts} \int d^3v i \mathbf{v}_{*s} \cdot \mathbf{k}_\perp v_\parallel \frac{F_{Ms}}{T_s} J_{0s}^2 \right\rangle + c.c. \\
&= \left\langle \int d^3v i \mathbf{v}_{*s} \cdot \mathbf{k}_\perp \delta f^*_{s\mathbf{k}_\perp} \frac{q_s}{2} (\phi_{\mathbf{k}_\perp} - v_{Ts} v_\parallel A_{\parallel \mathbf{k}_\perp}) J_{0s} + c.c. \right\rangle \\
&= \left\langle \frac{-ik_y}{2} \frac{T_s}{BL_n} \left[\int d^3v f^*_{s\mathbf{k}_\perp} \left(1 + (\frac{v_\parallel^2}{2} + \mu B - \frac{3}{2}) \eta_s \right) \phi_{\mathbf{k}_\perp} J_{0s} \right] \right\rangle + c.c. \\
&= \left\langle \frac{-ik_y}{2B} \left[\frac{1}{L_{Ts}} \left(\frac{\hat{p}^*_{\parallel s\mathbf{k}_\perp}}{2} + \hat{p}_{\perp s\mathbf{k}_\perp} - \frac{5}{2} \hat{n}^*_{s\mathbf{k}_\perp} \right) \phi_{\mathbf{k}_\perp} - T_s \left(\frac{1}{L_n} + \frac{1}{L_{Ts}} \right) \hat{n}^*_{s\mathbf{k}_\perp} \phi_{\mathbf{k}_\perp} \right. \right. \\
&\quad \left. \left. - \frac{1}{L_{Ts}} \left(\frac{\hat{q}^*_{\parallel s\mathbf{k}_\perp}}{2} + \hat{q}_{\perp s\mathbf{k}_\perp} \right) A_{\parallel \mathbf{k}_\perp} - T_s \left(\frac{1}{L_n} + \frac{1}{L_{Ts}} \right) \hat{u}^*_{\parallel s\mathbf{k}_\perp} A_{\parallel \mathbf{k}_\perp} \right] \right\rangle + c.c. \qquad \text{(C 2)} \\
&= \frac{\Theta_{es,s\mathbf{k}_\perp}}{L_{Ts}} + \frac{T_s \Gamma_{es,s\mathbf{k}_\perp}}{L_{ps}} + \frac{\Theta_{em,s\mathbf{k}_\perp}}{L_{Ts}} + \frac{T_s \Gamma_{em,s\mathbf{k}_\perp}}{L_{ps}}, \qquad \text{(C 3)}
\end{aligned}$$

where the diamagnetic velocity is given by Eq. 5.1. The fifth term, which is the nonlinear term, vanishes

$$\begin{aligned}
&\sum_{\mathbf{k}_\perp} h^*_{s\mathbf{k}_\perp} [\chi_s, h_s]_{\mathbf{k}_\perp} + c.c. \\
&= \sum_{\mathbf{k}_\perp, \mathbf{k}'_\perp, \mathbf{k}''_\perp} \delta_{\mathbf{k}_\perp, \mathbf{k}'_\perp + \mathbf{k}''_\perp} \mathbf{b} \cdot \mathbf{k}'_\perp \times \mathbf{k}''_\perp (\chi_{s\mathbf{k}'_\perp} h_{s\mathbf{k}''_\perp} h^*_{s\mathbf{k}_\perp} + \chi^*_{s\mathbf{k}'_\perp} h^*_{s\mathbf{k}''_\perp} h_{s\mathbf{k}_\perp}) \\
&= \sum_{\mathbf{k}_\perp, \mathbf{k}'_\perp, \mathbf{k}''_\perp} \delta_{\mathbf{k}_\perp, \mathbf{k}'_\perp + \mathbf{k}''_\perp} \mathbf{b} \cdot \mathbf{k}'_\perp \times \mathbf{k}''_\perp (\chi_{s\mathbf{k}'_\perp} h_{s\mathbf{k}''_\perp} h^*_{s\mathbf{k}_\perp} - \chi_{s\mathbf{k}'_\perp} h_{s\mathbf{k}''_\perp} h^*_{s\mathbf{k}_\perp}) \\
&= 0. \qquad \text{(C 4)}
\end{aligned}$$

This is because, by exchanging $\mathbf{k}$ and $\mathbf{k}''$ and using $\chi^*_{s\mathbf{k}'_\perp} = \chi_{s-\mathbf{k}'_\perp}$, the second term becomes

$$\sum_{\mathbf{k}_\perp,\mathbf{k}'_\perp,\mathbf{k}''_\perp} \delta_{\mathbf{k}''_\perp,\mathbf{k}'_\perp+\mathbf{k}_\perp} \mathbf{b}\cdot\mathbf{k}'_\perp \times \mathbf{k}_\perp \chi_{s-\mathbf{k}'_\perp} h^*_{s\mathbf{k}''_\perp} h_{s\mathbf{k}''_\perp}$$
$$= -\sum_{\mathbf{k}_\perp,\mathbf{k}'_\perp,\mathbf{k}''_\perp} \delta_{\mathbf{k}_\perp,\mathbf{k}'_\perp+\mathbf{k}''_\perp} \mathbf{b}\cdot\mathbf{k}'_\perp \times \mathbf{k}''_\perp \chi_{s\mathbf{k}'_\perp} h^*_{s\mathbf{k}_\perp} h_{s\mathbf{k}''_\perp}. \quad \text{(C 5)}$$

From the l.h.s. to the r.h.s. $\mathbf{k}_\perp$ is replaced to $-\mathbf{k}_\perp$ because $\sum_{\mathbf{k}_\perp} = \sum_{\mathbf{k}_\perp=-N_k}^{N_k}$ and, $\delta_{\mathbf{k}''_\perp,\mathbf{k}'_\perp-\mathbf{k}_\perp} \mathbf{b}\cdot\mathbf{k}'_\perp \times \mathbf{k}_\perp = \delta_{\mathbf{k}''_\perp,\mathbf{k}'_\perp-\mathbf{k}_\perp} \mathbf{b}\cdot\mathbf{k}'_\perp \times (\mathbf{k}_\perp{}' + \mathbf{k}_\perp{}'') = \delta_{\mathbf{k}_\perp,\mathbf{k}'_\perp+\mathbf{k}''_\perp} \mathbf{b}\cdot\mathbf{k}'_\perp \times \mathbf{k}_\perp{}''$ is used. The sixth term, which is the collision term, becomes

$$\left\langle \int d^3v \frac{T_s}{2F_{Ms}} h^*_{s\mathbf{k}_\perp} C_s(h_{s\mathbf{k}_\perp}) \right\rangle + c.c. = D_{s\mathbf{k}_\perp}. \quad \text{(C 6)}$$

Using Eqs. (C 1)-(C 6), we have the entropy balance equation Eq. (3.1).

Appendix D

Here it is shown that the dispersion relation of the high frequency mode in Sec. 4.3 can be derived by using a fluid model. We consider a collisionless plasma in a uniform magnetic field, which is the same as the previous appendix. We further assume that the plasma is uniform $\nabla F_{Ms} = 0$ which implies the diamagnetic drift velocity vanishes $\mathbf{v}_{*s} = 0$. Equation B 4 becomes

$$\frac{\partial}{\partial t}\delta f_{s\mathbf{k}_\perp} + v_{Ts} v_\parallel \mathbf{b}\cdot\nabla \delta f_{s\mathbf{k}_\perp} = v_{Ts} v_\parallel \frac{q_s}{T_s} F_{Ms} \mathbf{b}\cdot\nabla\phi_{\mathbf{k}_\perp} J_{0s}. \quad \text{(D 1)}$$

A set of gyro-fluid equations is derived by integrating Eq. (D 1) and Eq. (D 1) multiplied by $v_\parallel$ over the velocity space. The equations for the gyro-center density $\delta n_{s\mathbf{k}_\perp} = \int \delta f_{s\mathbf{k}_\perp} d^3v$ and the gyro-center parallel velocity $\delta u_{s\mathbf{k}_\perp} = \int v_\parallel \delta f_{s\mathbf{k}_\perp} d^3v$ are

$$\frac{\partial}{\partial t}\delta n_{s\mathbf{k}_\perp} = -v_{Ts}\mathbf{b}\cdot\nabla\delta u_{s\mathbf{k}_\perp}, \quad \text{(D 2)}$$

$$\frac{\partial}{\partial t} m_s \delta u_{s\mathbf{k}_\perp} = -v_{Ts}\mathbf{b}\cdot\nabla\left(\delta p_{\parallel s\mathbf{k}_\perp} + \frac{q_s}{T_s}\phi_{\mathbf{k}_\perp}\right), \quad \text{(D 3)}$$

respectively, where $\int F_{Ms} v_\parallel d^3v = 0$ is used. We assume a closure: $\delta p_{\parallel s\mathbf{k}_\perp} = 0$ and higher moments are zero. By using the Poisson equation Eq. 2.4 for long wavelength perturbations

$$\sum_s \left(q_s \delta n_{s\mathbf{k}_\perp} e^{-\rho^2_{Ts} k^2_\perp/2} - \frac{q_s^2}{T_s}(1-\Gamma_{0s})\phi_{\mathbf{k}_\perp} \right) = 0, \quad \text{(D 4)}$$

we have

$$\frac{\partial}{\partial t}\sum_s \frac{q_s^2}{T_s}(1-\Gamma_{0s})\phi_{\mathbf{k}_\perp} = -q_e v_{Te}\mathbf{b}\cdot\nabla\delta u_{e\mathbf{k}_\perp} e^{-\rho^2_{Te}k^2_\perp/2}, \quad \text{(D 5)}$$

$$\frac{\partial}{\partial t} m_e \delta u_{e\mathbf{k}_\perp} = -v_{Te}\mathbf{b}\cdot\nabla\frac{q_e}{T_e}\phi_{\mathbf{k}_\perp}, \quad \text{(D 6)}$$

where the ion parallel velocity is neglected $\delta u_{i\mathbf{k}_\perp} = 0$ because $v_{Ti} \ll v_{Te}$. The dispersion relation of a wave in the plasma is

$$k_\parallel^2 - \omega^2 m_e \sum_s \frac{q_s^2}{T_s}(1 - \Gamma_{0s}) = 0. \tag{D 7}$$

When we consider a wave with the typical wavelength comparable to that of ITG mode $k_\perp < 1/\rho_{Ti} \ll 1/\rho_{Te}$, we can approximate $\Gamma_{0e} \approx 1$ and $\Gamma_{0i} \approx 1 - \rho_{Ti}^2 k_\perp^2$, then we have $k_\parallel^2 = \omega^2 m_e k_\perp^2 \rho_{Ti}^2$. By rewriting to the dimensional form, we have the dispersion relation for the high frequency mode in Sec. 4.3

$$\omega^2 = \frac{k_\parallel^2}{k_\perp^2}\frac{m_i}{m_e}\Omega_{Ti}^2. \tag{D 8}$$